Soil Dynamics and Earthquake Engineering **12** (1993) 363–382

Long period Fourier amplitude spectra of strong motion acceleration

M.D. Trifunac

Civil Engineering Department, University of Southern California, Los Angeles, California 90089-2531, USA

Communicated by J. Enrique Luco

(Received 5 October 1992; revised version received 18 June 1993; accepted 16 July 1993)

The empirical equations for scaling Fourier amplitude spectra in the frequency band from ~0·1 to 25 Hz can be extrapolated to describe the long period strong motion amplitudes. The results of this extrapolation can agree with (1) the seismological and field estimates of permanent ground displacement (near field), and with (2) the independent estimates of seismic moment and the observed frequencies of far field Fourier spectrum amplitudes.

NOTATION

a Empirical scaling coefficient in description of the fault length $L = a \times 10^{bM}$;

$\mathscr{A}_0(T)$ Parabola w.r.t. $\log_{10} T$ which defines the frequency dependent attenuation in $\Delta^{\mathscr{A}_0(T)}$ (see eqn (2));

$$\mathscr{A}_0(T) = \begin{cases} -0{\cdot}732 & T \geq 1.8\,\text{s} \\ a + b\log_{10} T + C(\log_{10} T)^2 & T < 1.8\,\text{s} \end{cases}$$

where

$$a = -0{\cdot}767,\ b = 0{\cdot}271$$

and

$c = -0{\cdot}526$ (Trifunac and Lee[1])

$\mathscr{A}tt(\Delta, M, T)$ A function describing the frequency dependent ($f = 1/T$) attenuation of the spectral amplitudes versus distance Δ and magnitude M (is defined by eqn (2));

a_{NF}, a_{FF} A function describing the contribution of near-field ($a_{NF} = e^{-\frac{3S_1}{4S}}$) and of far-field spectra ($a_{FF} = 1 - e^{-\frac{3S_1}{4S}}$) to the Fourier amplitude spectra of strong motion acceleration, $FS(T)$

A Fault area, $A = WL$ (km^2)

b Empirical scaling coefficient in $L = a \times 10^{bM}$

$b_i(T)$ Empirical scaling 'coefficients' in eqn (1)

$b_i^{(j)}(T)$ Empirical scaling coefficients in eqn (1) for the indicator variable j

c Empirical scaling coefficient in $W = c \times 10^{dM}$

C_0 Scaling 'coefficient' relating the average fault displacement, $\bar{d}$, or the average fault dislocation, $\bar{u}$ ($\bar{u} = 2\bar{d}$), with the source dimensions r and the rigidity of the surrounding rocks, μ

C_0^* Proposed 'average' trend of C_0 versus M (see Tables 3 and 6)

C_s A scaling constant (see eqns (24) and (25))

d Empirical scaling coefficient in $W = c \times 10^{dM}$

d_p Permanent ground displacement, $d_p = d_{NF}(t)$, for $t \to \infty$

$d(t)$ Displacement of the ground motion versus time

$d_{NF}(t)$ Near-field strong motion displacement (for $\Delta < S$)

$d_{FF}(t)$ Far-field strong motion displacement (for $\Delta \gg S$)

$\bar{d}$ Average of $d_{NF}(t)$, for $t \to \infty$, on the fault surface

$D(\bar{M}_L^{SM})$ Difference between M_L^{SM} and M_p

Soil Dynamics and Earthquake Engineering 0267-7261/94/$07.00

E_s Seismic energy

f Frequency (Hz); also used as a coefficient in $W = e + fM$

f_1 Corner frequency, $f_1 = (\frac{L}{v} + T_0)^{-1}$ (Hz)

f_2 Corner frequency, $f_2 = 2{\cdot}2/W$ (Hz)

f_p Frequency where $FS(f)$ has peak amplitude (see Fig. 1)

f_{co} Frequency $(=1/T(N_c))$ below which eqn (1) is not valid (see Table 2)

f_{max} High frequency corner or cut-off frequency

$FS(T)$, $FS(\omega)$, $FS(f)$ Fourier amplitude spectrum of strong motion acceleration at period T, circular frequency ω, or frequency f

$FS_{NF}(\omega)$, $FS_{NF}(T)$, $FS_{FF}(\omega)$, $FS_{FF}(T)$ Fourier amplitude spectra of near-field and far-field strong motion acceleration, at frequency ω, or period T

G4RM Group of four regression models. Model 4 is shown in eqn (1). (1. MAG-SITE; 2. MAG-DEPTH; 3. MAG-SITE-SOIL; 4. MAG-DEPTH-SOIL)

h Depth (thickness) of the sedimentary layer beneath the station (km)

h_0 Depth (below the surface) of the top edge of a vertical fault plane (km)

H Focal depth (km)

k Slope of $\log_{10} M_0$ versus M (see eqn (28))

L, L_{min} Fault length and minimum fault length (km)

M Magnitude

M_* Cut off magnitude

M_{min}, M_{max} Minimum and maximum magnitudes defining the range $M_{min} < M < M_{max}$ where the strong motion amplitudes begin to saturate. For $M > M_{max}$, $FS(T)$ in eqn (1) is constant, i.e. does not grow with M

M_0 Seismic moment $(=\mu\bar{u}A)$ (dyne cm)

M_0^{SM} Seismic moment computed from strong motion data

M_L The local magnitude scale (Richter[2])

M_L^{SM} Local magnitude computed from strong motion accelerograms

M_p 'Magnitude' as published in various catalogues (without specification of the wave type used, or the procedure employed)

M_s Surface wave magnitude

$p(\epsilon, T)$ Probability density function describing the distribution of $\epsilon(T)$ in eqn (7)

Q The quality factor

r The characteristic source dimension (see Table 3) (km)

R Epicentral distance (km)

R_0 Transition distance where the frequency dependent attenuation $\mathcal{A}tt(\Delta, M, T)$ becomes $\sim R/200$ as in $\log_{10} A_0(R)$ (Richter[2])

s The geologic site condition parameter ($s = 0$ for sediments, $s = 2$ for basement rock and $s = 1$ for intermediate sites)

s_L A parameter describing the local soil site condition ($s_L = 0$ for 'rock' sites, $s_L = 1$ stiff sites, and $s_L = 2$ for deep soil sites)

S The source dimension used in eqn (3) and defined by eqn (4). Also used in eqn (26); the 'source dimension' $S = 0{\cdot}01 \times 10^{0{\cdot}5M}$ (km)

$S_L^{(1)}$, $S_L^{(2)}$ Indicator variables describing the local soil conditions (see eqn (5))

S_0 The coherence radius (Gusev[3]) of the source (km)

S_1 Distance between the station and the top of a vertical fault (km)

t Time (s)

t' Delayed time, $t' = t - R/\beta$

T Period of vibration, $T = 1/f$ (s)

$T(N)$ Periods $(N = 1, 2, \ldots, 12)$ for which $b_i(T)$, M_{min}, M_{max}, $\mu(T)$ and $\sigma(T)$ are prescribed in Table 1. Equation (1) can be used for $N < N_c$ (see Table 2), i.e. for $T < T(N_c)$

T_p Period where $FS(T)$ is maximum, $T_p = 1/f_p$

T_c Cut off period $T_c = T(N_c) = 1/f_{co}$ (see Table 2)

T_0 The dislocation rise time, $T_0 \sim \frac{\bar{u}\mu}{\sigma\beta}$ (s)

u, u_{max} Dislocation amplitude, maximum dislocation amplitude

$\bar{u}$ Dislocation averaged over the fault surface

v Dislocation velocity (km/s)

V An indicator variable; $V = 0$ for horizontal motion, $V = 1$ for vertical motion

$W, W_{\min}, W_*$	Fault width, minimum fault width, a distance such that $W = \xi W_*$, for $0 < \xi < 1$ (km)
α	Corner frequency in the Brune's spectrum (see eqn (16))
α_0	Scaling constant (in $\bar{u} = \alpha_0 L$)
β	Velocity of shear waves, $\beta = (\mu/\rho)^{1/2}$ (km/s)
Δ	The 'representative' source to station distance (see eqn (3))
$\epsilon(T)$	Residuals, $\epsilon(T) = \log_{10} FS(T) - \log_{10} \widehat{FS}(T)$ (see eqn (6))
η	The efficiency in the expression for the apparent stress, $\eta\bar{\sigma}$
μ	Shear modulus, $\mu = \rho\beta^2$ (dyne/cm^2)
$\mu(T)$	The mean of distribution $p(\epsilon, T)$
π	Constant (=3·14159)
ρ	Material density (g/cm^3)
σ	Effective stress (also used as stress drop, Brune,[4] defined as the difference of stress before the earthquake and the frictional stress during faulting
$\sigma(T)$	Standard deviations of the distribution $p(\epsilon, T)$ in eqn (7)
τ	The characteristic source time, $\tau = 1/f_1 = \frac{L}{v} + T_0$
ω	Circular frequency, $\omega = 2\pi f$ (rad/s)
ω_1, ω_2	Corner frequencies $\omega_1 = 2\pi f_1$, $\omega_2 = 2\pi f_2$ (rad/s)
$\Omega_{NF}(\omega), \Omega_{FF}(\omega)$	Near-field and far-field Fourier amplitude spectra of strong motion displacement

INTRODUCTION

Since the 1960s and the early 1970s, following the pioneering works of Haskell[5,6] and Brune,[4] numerous studies and interpretations were published dealing with spectral representation of the physical processes at the earthquake source.[7] From those, we learned that the corner frequencies in the observed far-field spectra can be associated with the characteristic source dimensions, that the high frequency fall-off of ground displacement amplitudes, beyond the corner frequency, can be described by ω^{-n} (where n is in the range between 2 and 3), and that the zero frequency spectral amplitudes can be related to the seismic moment [8] M_0. During the following 20 years, many papers were published on (1) the physical interpretations of the processes at the earthquake source and their influence on the shape and amplitudes of the far-field displacement spectra, (2) the simple source characteristics as determined by the measured features of the observed far-field spectra, and (3) the use of the inferred source characteristics and the statistics of the observed source parameters to predict spectra of future strong and distant ground motion.

Simultaneously, in earthquake engineering, the strong motion data base was growing, and the first studies of the near field spectral characteristics using strong motion accelerograms at distances typically less than 100 km could be carried out.[9] At present, detailed empirical equations are available to describe the Fourier amplitude spectra of strong motion acceleration in the frequency range from ~0·1 to 25 Hz and for distances between about 10 and 100 km.[10,11]

The purpose of this paper is to address the following two questions: (1) is it possible to extrapolate the empirical equations for scaling Fourier amplitude spectra of strong ground motion, near the source, to frequencies $f < 0{\cdot}1$ Hz, and (2) can the thus extrapolated spectral amplitudes satisfy the observations in the near field and at intermediate and teleseismic distances. The engineering need for such information continues to grow with the design of long bridges, fluid storage tanks, large dams and long tunnels, for example. Also, providing consistent and continuous spectral representation of earthquake wave amplitudes for long period motions and from small to large distances, should help in the studies and in the use of distant spectral amplitudes. Compared to distant seismological recordings, the earthquake ground motion recorded by strong motion accelerographs contains fairly complete and reliable information on the earthquake source, because the scattering, diffraction, geometrical spreading, and inelastic attenuation are smaller along a shorter wave path. The proximity to the source offers more detailed, direct and more complete data on strong ground motion, and thus can be used to (1) check and calibrate the distant recordings, and (2) learn more about the high frequency features of the earthquake source.

Most of the seismological studies either assume directly functional forms for the spectral amplitudes (for example, following the Brune's[4] shear wave spectra[12–15]), or assume a source model resulting in a functional form which determines these spectral estimates.[3,16–18] These models are specified by the following scaling parameters: seismic moment, M_0, one or two long period corner frequencies (f_1 and f_2 which are inversely proportional to the source dimensions), some form of stress drop on the fault plane, and the low-pass filtering characteristics of the surrounding medium ($f_{\max}$, Hanks[19]) or the non-linear phenomena at the tip of a propagating dislocation.[20] Since M_0 determines the long period spectral amplitudes, while the stress drop characterizes the high frequencies, such models provide means to interpolate the spectral behavior for the intermediate frequency band. However, the func-

tional form of these spectral amplitudes is typically based only on the body wave spectra. Therefore, it cannot be expected that these models will approximate the Fourier amplitude spectra of a complete strong motion signal in the near and intermediate field. In the end, these results can be 'calibrated', in part, using recorded strong motion data,[3,15] but their 'accuracy' finally depends on one's ability to predict M_0 and the stress drop.

In contrast, this study uses regression equations of actually recorded strong motion data (in the western USA and mainly in California) to estimate the Fourier amplitude spectra for the intermediate frequency band (from $\sim 0{\cdot}1$ to 25 Hz). Our regression equations do have terms which can be attributed to the processes at the earthquake source, the attenuation along the wave path and the observed ground motion in general. However, the final regression models contain only the statistically significant terms, i.e. those terms with coefficients and coefficient functions significantly different from zero in the frequency band considered. In this paper, the author does not modify these equations, but merely explores how they can be extrapolated to lower ($f \leq 0{\cdot}1$ Hz) frequencies.

The extrapolated spectra of strong motion acceleration are represented as a linear combination of a near-field (FS_{NF}) and a far-field (FS_{FF}) term (as $a_{NF} FS_{NF}(\omega) + a_{FF} FS_{FF}(\omega)$, with coefficient functions such that $a_{NF} + a_{FF} = 1$). The near-field and the far-field extensions are obtained as follows. The functional form for the shape of the extrapolated near-field spectra, $FS_{NF}(\omega)$, is defined using earthquake source theory. Then, the final amplitudes of the extrapolated near-field spectra are determined by matching with the corresponding empirical amplitudes (defined by the regression equation) at the longest period for which the empirical equation can be relied on. For the shape of the extension of the far-field spectra, $FS_{FF}(\omega)$, functions are used which are similar to the body wave spectra in the Haskell[6] source model. Then, the amplitudes of the extrapolated far-field spectra are determined also by matching with the amplitudes of the empirical spectra (at the longest period for which the empirical equation are reliable). The final far-field and near-field extended spectra have continuous amplitudes at the matching period, but not necessarily continuous slopes. At the end, the success of this approach is tested by estimating various source and strong motion characteristics (permanent displacements, seismic moment, M_0, fault dimensions, corner frequencies, f_1 and f_2, characteristic source duration and fault area) using the extrapolated spectral amplitudes, and then comparing these estimates with independent measurements of the same quantities.

STRONG MOTION DATA

The strong motion acceleration data base started to grow from March 10, 1933, when the first strong motion accelerograms were recorded during the Long Beach ($M = 6{\cdot}3$), earthquake in California. The San Fernando, California earthquake of February 9, 1971, contributed the first major increment to the strong motion data base. After all the accelerograms were digitized, together with selected older recordings from the period between 1933 and 1971, 186 uniformly processed free-field strong motion records were available.[21,22] Following the Imperial Valley, in 1979, the Coalinga in 1983, and the Morgan Hill in 1984, earthquakes in California, the uniformly processed strong motion data base more than doubled, to 493 uniformly processed records. With the recent recordings by the Los Angeles strong motion array (1987–1992) and following the 1989 Loma Prieta, California, earthquake, when all these data are uniformly processed, there will be well over 1000 excellent records in the strong motion data base.

EMPIRICAL SCALING EQUATIONS

The most recent equation for the empirical scaling of Fourier amplitude spectra of acceleration, $FS(T)$, is of the form

$$\begin{aligned}\log_{10} FS(T) = {} & M + \mathscr{A}tt(\Delta, M, T) + b_1(T)M \\ & + b_2(T)h + b_3(T)V + b_4(T)hV \\ & + b_5(T) + b_6(T)M^2 + b_7^{(1)}(T)S_L^{(1)} \\ & + b_7^{(2)}(T)S_L^{(2)} \end{aligned} \tag{1}$$

where M is the earthquake magnitude,[2,23,24] $b_1(T)$–$b_7^{(2)}(T)$ are scaling coefficient functions of the period T, and $\mathscr{A}tt(\Delta, M, T)$ is the frequency dependent attenuation function,[25]

$$\mathscr{A}tt(\Delta, M, T) = \begin{cases} \mathscr{A}_0(T)\log_{10}\Delta; & R \leq R_0 \\ \mathscr{A}_0(T)\log_{10}\Delta_0 - (R - R_0)/200; & R > R_0 \end{cases} \tag{2}$$

with Δ, the 'representative' source to station distance,

$$\Delta = S \ln \left[\frac{R^2 + H^2 + S^2}{R^2 + H^2 + S_0^2} \right]^{1/2} \tag{3}$$

R is the epicentral distance and H is the focal depth, both in kilometers. R_0 is the transition distance[25] (about 150 km for $T < 0{\cdot}05$ and ≈ 50 km for $T > 1$ s) beyond which the attenuation equation has a slope equal to 1/200, and Δ_0 is the value of Δ in eqn (3) when $R = R_0$. $\mathscr{A}tt(\Delta, M, T)$ depends on M implicitly, through S, which is the linearized 'source dimension'

$$S = 0{\cdot}2 + 8{\cdot}51(M - 3), \quad \text{for } M > 3 \tag{4}$$

S_0 is the coherence radius of the source[3] and is

approximated by $S_0 \sim \beta T/2$, where β is the shear wave velocity in the source region, and T is the period of motion. When S/R and S_0/R become small, $\Delta \to (R^2 + H^2)^{1/2}$, which is the hypocentral distance to the source. $\mathscr{A}_0(T)$ in eqn (2) is represented by a parabola (in $\log_{10} T$), between $T = 0{\cdot}04$ and $1{\cdot}8$ s. It is near -2 for $T = 0{\cdot}04$, it increases to $\sim -0{\cdot}7$ and remains constant for $T > 1{\cdot}8$ s.[1]

The thickness of the sedimentary layer is h, extending from the ground surface to the basement rock (in kilometers). $V = 0$ is for horizontal motion and $V = 1$ is for vertical motion. The term $b_4(T)hV$ models the progressively steeper incidence of body waves for soft and deeper sedimentary sites. $b_1(T)M$ and $b_6(T)M^2$ model the saturation of strong motion amplitudes versus M, for $-b_1(T)/(2b_6(T)) \equiv M_{\min} < M < M_{\max} \equiv -(1 + b_1(T))/(2b_6(T))$. $S_L^{(1)}$ and $S_L^{(2)}$ are indicator variables defined by

$$S_L^{(1)} = \begin{cases} 1 & \text{if } s_L = 1 \text{ (stiff soil)} \\ 0 & \text{otherwise} \end{cases} \qquad (5)$$

$$\text{and} \quad S_L^{(2)} = \begin{cases} 1 & \text{if } s_L = 2 \text{ (deep soil)} \\ 0 & \text{otherwise} \end{cases}$$

where $s_L = 0$, 1 and 2 represent 'rock', stiff soil and deep soil sites. The sites with soft to medium clays with strata of sands and gravels, as defined in the original investigation by Seed *et al.*,[26] are not common in the Western United States and are therefore not considered in this analysis.

With $\widehat{FS}(T)$ representing the Fourier amplitude spectra estimated from eqn (1), and $FS(T)$ indicating the spectra computed from recorded accelerograms, the residues $\epsilon(T)$ can be calculated from

$$\epsilon(T) = \log_{10} FS(T) - \log_{10} \widehat{FS}(T) \qquad (6)$$

$\epsilon(T)$ can be described as a normal random variable with a cumulative probability distribution function $p(\epsilon, T)$, mean $\mu(T)$ and standard deviation $\sigma(T)$. Then,

$$p(\epsilon, T) = \frac{1}{\sigma(T)\sqrt{2\pi}} \times \int_{-\infty}^{\epsilon(T)} \exp\left[-\frac{1}{2}\left(\frac{x - \mu(T)}{\sigma(T)}\right)^2\right] dx \qquad (7)$$

is the probability that $\log_{10} FS(T) - \log_{10} \widehat{FS}(T) \leq \epsilon(T)$. Table 1 gives $b_1(T)$–$b_7^{(2)}(T)$, $M_{\min}$, $M_{\max}$, $\mu(T)$ and $\sigma(T)$ at 12 periods $T(N)$, $N = 1, 2, \ldots, 12$, between $T(1) = 0{\cdot}04$ and $T(12) = 14{\cdot}0$ s.

The first empirical model for scaling $\log_{10} FS(T)$ that involves the frequency dependent attenuation $\mathscr{A}tt(\Delta, M, T)$ was developed in 1985, but without explicit consideration of the soil site parameters s_L.[1,27,28] Simultaneously with that analysis and with the model described above by eqn (1), we studied also the geologic site conditions using $s = 0$, 1 and 2, in place of h (see Trifunac and Brady,[29] for definition and examples of site characterization with s, and Seed *et al.*[26] for definition and examples of assigning s_L). The reader may wish to peruse the details on how these models have evolved, starting with our analysis in 1976,[21] but for the purposes of this paper it will suffice to recognize only the four most recent models:

1. MAG-SITE Model,[1]
2. MAG-DEPTH Model,[1]
3. MAG-SITE-SOIL Model,[1] and
4. MAG-DEPTH-SOIL Model[10]
   (eqn (1) and Table 1).

In what follows, these four models will be used collectively, and will be referred to as the 'group of four recent scaling nodels' (G4*RM*). In the above, 'MAG' implies scaling in terms of earthquake magnitude, 'SITE' indicates the use of the geological site parameters $s = 0$, 1 or 2, and 'DEPTH' implies the use

Table 1. $\mathbf{Log_{10}\ FS(T) = M_< + \mathscr{A}tt(\Delta, M, T) + b_1(T)M_{<>} + b_2(T)h + b_3(T)V + b_4(T)hV + b_5(T) + b_6(T)M_{<>}^2 + b_7^{(1)}(T)S_7^{(2)} + b_L^{(1)}(T)S_L^{(2)}}$

$N =$	1	2	3	4	5	6	7	8	9	10	11	12
Period, T (s)	0·040	0·065	0·11	0·19	0·34	0·50	0·90	1·60	2·80	4·40	7·50	14·0
Coefficients												
$b_1(T)$	0·652	0·667	0·819	0·962	0·977	0·927	0·854	0·876	0·940	0·856	0·382	−0·707
$b_2(T)$	0·067	0·063	0·056	0·047	0·040	0·039	0·049	0·067	0·084	0·087	0·069	0·020
$b_3(T)$	0·127	0·091	−0·012	−0·155	−0·272	−0·292	−0·233	−0·152	−0·122	−0·126	−0·132	−0·131
$b_4(T)$	0·006	−0·002	−0·015	−0·030	−0·041	−0·047	−0·051	−0·048	−0·040	−0·033	−0·030	−0·034
$b_5(T)$	−3·921	−3·876	−4·151	−4·532	−4·809	−4·924	−5·151	−5·568	−5·881	−5·529	−3·791	−0.019
$b_6(T)$	−0·095	−0·098	−0·114	−0·127	−0·128	−0·123	−0·112	−0·110	−0·113	−0·110	−0·080	−0·006
$b_7^{(1)}(T)$	−0·314	−0·282	−0·219	−0·120	−0·008	0·052	0·120	0·161	0·161	0·127	0·065	−0·002
$b_7^{(2)}(T)$	−0·264	−0·260	−0·238	−0·151	−0·012	0·069	0·144	0·169	0·152	0·103	0·004	−0·144
$M_{\min}$	3·429	3·389	3·604	3·780	3·810	3·773	3·814	3·991	4·155	3·897	2·376	0·000
$M_{\max}$	8·691	8·472	8·006	7·711	7·711	7·845	8·282	8·549	8·576	8·450	8·600	14·500
$\mu(T)$	−0·002	−0·002	−0·002	−0·001	−0·001	−0·001	−0·002	−0·001	0·002	0·003	0·001	−0·001
$\sigma(T)$	0·445	0·462	0·388	0·343	0·316	0·317	0·338	0·352	0·343	0·328	0·315	0·305

$M_< = \min(M, M_{\max})$, $M_{<>} = \max(M_{\min}, M_<)$.

of h as in eqn (1) above. 'SOIL' shows that the soil site parameters $s_L = 0$, 1 and 2 are used in the scaling equation. In the models 1 and 2 such dependence is omitted.

The need to consider different scaling models (1–4) results from the lack of data on local site conditions. Which of the four models in the G4*RM* will be used, will depend on whether some or all the site parameters (s, h, s_L) are available, and on various constraints on the scaling parameters imposed by other aspects of a site specific analysis. To illustrate the resulting differences between these models, in most calculations and figures in this paper, all the four models are used. To simplify the figures, and to distinguish this from the differences in the results caused by the four models of fault geometry (W and L in Table 5 (later)), only the range of values resulting from the models 1–4 in the G4*RM*, will be shown by a shaded zone and usually for probabilities of exceedance equal to 0·1, 0·5 and 0·9.

Figure 1 illustrates $\log_{10} FS(T)$ plotted versus frequency, $f = \frac{1}{T}$. The dashed lines show the empirical Fourier amplitude spectra, determined by eqn (1), for 50% probability of exceedance (corresponding to $p(\epsilon, T) = 0{\cdot}5$ in eqn (7)), and for magnitudes $M = 4$, 5, 6, 7 and 8 (from bottom to top), at epicentral distance $R = 10$ km, and for source depth $H = 0$ km. The shortest frequency for which the empirical scaling equations are reliable (the cut-off frequency) is denoted by f_{co} and is marked by the symbol '○' in Fig. 1. The cut-off frequency is larger for smaller magnitudes and for larger source to station distances, i.e. the empirical spectra are valid for progressively shorter frequencies as the magnitude and the source to station distance increase. This is caused by the recording and processing noise,[31–35] whose amplitudes are shown in the same figure by the rectangular shaded zone (increasing from $FS \sim 10^{-1}$ in/s for $f \sim 10$ Hz, to $FS \sim 1$ in/s near

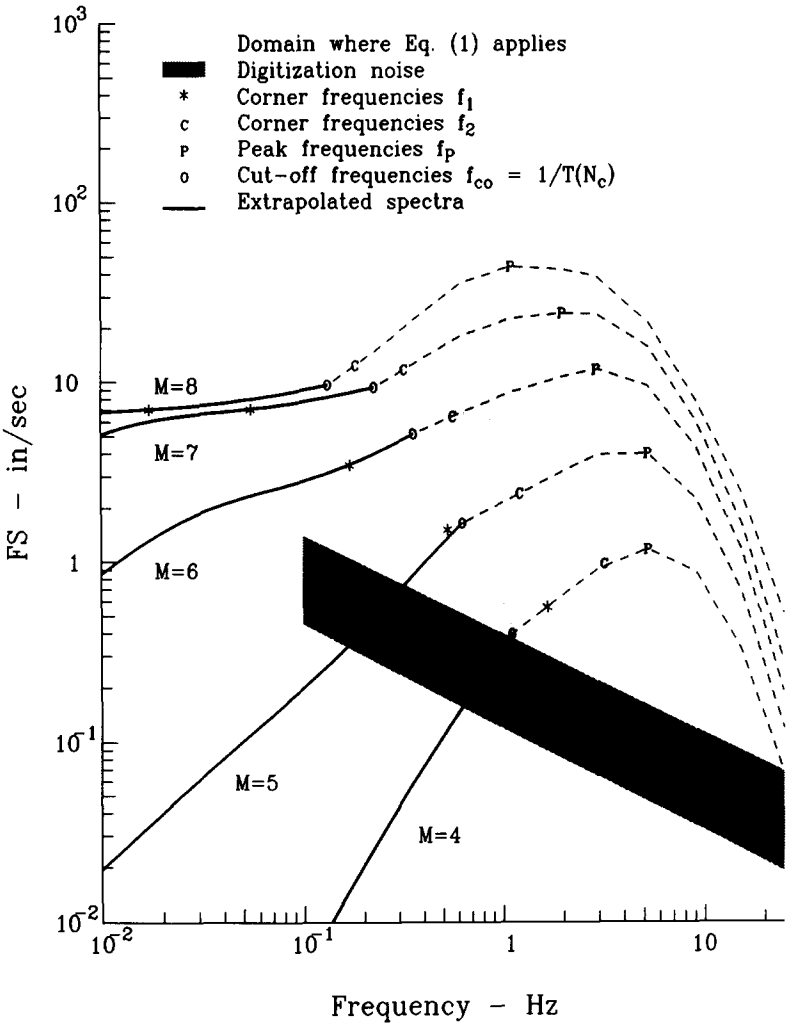

Fig. 1. Fourier amplitude spectra (in/s) versus frequency (Hz), for probability of exceedance equal to 0·5, for $M = 4$, 5, 6, 7 and 8 (bottom to top), at epicentral distance $R = 10$ km, and for a source at depth $H = 0$. Outside the shaded region, between $f_{co} = 1/T(N_c)$ and $f = 25$ Hz where eqn (1) is valid, the spectral amplitudes (heavy solid lines) can be extrapolated to $f < f_{co}$ as it is suggested in this paper (see eqn (27)). The corner frequencies f_1, f_2 and f_{co} are defined in the text. The processing and digitization noise amplitudes are shown by the shaded zone increasing from $FS \approx 10^{-1}$ to $FS \approx 1$ in/s for frequencies decreasing from 10 to 0·1 Hz.

Table 2. Cut-off periods $T(N_c)$ versus magnitude

M	$T(N_c)$	N_c
3	0·90	7
4	0·90	7
5	1·60	8
6	2·80	9
7	4·40	10
8	7·50	11

$f = 0{\cdot}1$). At the high frequency end, the empirical spectra are defined only up to 25 Hz, this limit being chosen more for convenience in data processing than because of poor signal to noise ratio. The top shaded area in Fig. 1 shows the region where the empirical eqn (1) is valid. Table 2 shows the cut-off periods, $T(N_c) = 1/f_{co}$, versus magnitude (neglecting the dependence of f_{co} on distance). For uniformity, all the G4*RM* empirical equations are defined for 12 periods $T(N)$, $N = 1, \ldots, 12$, listed in the first row of Table 1, but these can be used only for periods with index $N \leq N_c$ (listed in Table 2).

In what follows, the spectral amplitudes will be extrapolated to low frequencies, starting at the 'end frequency' f_{co} (end period $T(N_c)$) of the spectra (the left border of the top gray zone), as shown in Fig. 1 by the heavy solid lines. Also, all the spectra and the analyses will be based on the estimates of strong ground motion at sites on basement rock (geologic site condition number $s = 2$ or depth of sediments $h = 0$) and on 'rock' soil sites (soil site number $s_L = 0$; in geotechnical literature on earthquake engineering, the sites on deposits with shear wave velocity higher than 800 m/s, or with thickness less than 10 m, are referred to as 'rock' sites). This will eliminate complications introduced by the local site conditions[36] and will allow more direct comparison with seismological studies and observations. Without loss of generality, the results of eqn (1) will be used for horizontal motions only ($V = 0$) to simplify further the presentation and interpretation of these empirical equations.

LOW FREQUENCY EXTENSION

In the proposed extrapolation, two separate cases will be considered. In the first case, the recording site is so close to the earthquake source that the ground will experience permanent static displacement after an earthquake. This will occur when the site is close to the fault surface, at a distance smaller than the characteristic source dimension. One can refer to this case as the 'near-field' ground motion. In the second case, the recording station is far from the source, so that the contributions from the static displacement are negligible, that is, all near and intermediate field terms,[6] attenuating as R^{-4} and R^{-2}, have become negligible, and only the body waves (attenuating like R^{-1}) and the surface waves (attenuating like $R^{-1/2}$), where R is the source to station distance, will contribute to the strong motion amplitudes. By using a suitable linear combination, with scaling functions a_{NF} and a_{FF} (both a_{NF} and a_{FF} will depend on distance, source dimension, source depth and source size, via magnitude), such that $a_{NF} + a_{FF} = 1$, in the end, Fourier amplitude spectra of strong motion acceleration will be proposed in the period range $T > T(N_c)$ valid for all distances. The spectral amplitude evaluated at $T = T(N_c)$ by eqn (1) will be used as a starting point for both the near-field, $F_{NF}(\omega)$, and far-field, $F_{FF}(\omega)$, spectra of strong motion acceleration.

Near-field displacements

Following Brune,[4] the near-field displacement, $d_{NF}(t)$, is represented by

$$d_{NF}(t) = d_p(1 - e^{-t/\tau}) \tag{8}$$

where d_p is the static displacement at the station (on the ground surface) following the earthquake, t is the time, and τ is the characteristic time, which will be related to the duration of the faulting. The real details of ground motion, of course, are more complicated. When the observation point is on the fault surface, the average of d_p can be described by

$$\bar{d} = \frac{1}{2} C_0 \frac{\sigma r}{\mu} \tag{9}$$

where σ is the effective[4] stress drop, r is the equivalent (radius) dimension of the source area and μ is the rigidity in the source region (typically in the range from 1 to 5×10^{11} dynes/cm^2). C_0 is a 'constant' which depends on the type of faulting and is in the range from 0·4 to 1·6 (Table 3). The factor of 1/2 in eqn (9) relates the displacement of a point (d_p) to the average source dislocation amplitude $\bar{u}$, which for symmetric faulting is $2\bar{d}$. The bars on u and d designate average values.

As the area of the fault surface, LW (L is fault length, and W is the fault width), increases with increasing magnitude, W becomes larger and u_{max} is located at progressively greater depths. Detailed source mechanism studies in California for the earthquakes which have contributed to the strong motion data base used here, suggest that the largest dislocation amplitudes do not occur near the ground surface.[40–47] During the Parkfield earthquake of 1966, the dislocation apparently occurred at depth[48] and its eventual surface expression grew through creep for about 1 year following the earthquake. For the purposes of this analysis, we need d_p (on the ground surface), and since sufficient data are not available on the average displacement, $\bar{d}$, versus magnitude, faulting mechanisms, fault types and on the distribution of rigidities and stresses on the two sides of the fault,[49] it is assumed that the average of d_p can be approximated[50,51] by

$$\bar{d} \sim \frac{3\bar{u}}{8} \tag{10}$$

Table 3. $\bar{u} = C_0 \sigma r/\mu$, $\bar{u} = 2\bar{d}$

Type of faulting and fault geometry	C_0	r represents
Dip-slip displacement along an infinitely long narrow strip in a uniform shear field[37]	$\frac{3\pi}{16}$	Fault width
Infinitely long vertical surface fault with strike slip displacement[38]	$\frac{\pi}{2}^a - \frac{\pi}{4}^b$	Fault width
Circular fault plane in an infinite medium	$\frac{8}{7\pi}^c$	Diameter of circular dislocation (fault width)

Note: To model the assumed 'continuous' changes of the faulting type and geometry, for the body of strong motion data studied here, will be defined $C_0^* = 0{\cdot}4$, $0{\cdot}5$, $0{\cdot}65$, $0{\cdot}85$, $1{\cdot}6$ and $1{\cdot}6$ for earthquake magnitudes $M = 3$, 4, 5, 6, 7 and 8. $C_0^* = 0{\cdot}4$ is representative of small 'circular' faults, while $C_0^* = 1{\cdot}6$ will represent long surface faults.
[a] Surface fault.
[b] Deep fault.
[c] Poisson ratio, $\nu = 0{\cdot}25$.

The Fourier amplitude spectrum of $d_{NP}(t)$ in eqn (8) is

$$\Omega_{NF}(\omega) = \frac{d_p}{\tau\omega} \frac{1}{(\omega^2 + \tau^{-2})^{1/2}} \tag{11}$$

When $\omega \to 0$, $\Omega_{NF}(\omega) \to d_p/\omega$. Using the approximate relationship between d_p and $\bar{u}$ in eqn (10), this implies that

$$\bar{\Omega}_{\substack{NF \\ \omega \to 0}} \to \approx \frac{3}{8} \frac{\bar{u}}{\omega} \tag{12}$$

The fluctuations of d_p on the ground surface are considerable, and will depend on the relative position of the observation point with respect to the fault surface and the three-dimensional properties of the geologic medium surrounding the fault. Since here we are dealing with empirical scaling of Fourier spectrum amplitudes, and because our model equations (e.g. eqn (1)) represent the average trends for many observations, for the purposes of this analysis, it will suffice to deal with the average trends of d_p as in the above equations.

For Fourier amplitude spectra of strong motion acceleration in the near field, $FS_{NF}(\omega)$, eqn (11) gives

$$FS_{NF}(\omega) = \frac{\omega d_p}{[(\omega\tau)^2 + 1]^{1/2}} \tag{13}$$

where τ can be approximated by $\tau \sim r/\beta$ (β is the velocity of shear waves) when $r < W/2$. When $L \gg W$,

$$\tau \approx \frac{L}{v} + T_0$$

where v is the average velocity with which the dislocation propagates along the fault length, and T_0 is the dislocation rise time.[6] For $\frac{L}{v} \gg T_0$, we can define one of the corner frequencies by

$$f_1 = \frac{\omega_1}{2\pi} \sim \frac{v}{L}$$

For intermediate frequencies

$$f_1 = \left[\frac{L}{v} + T_0\right]^{-1}$$

with a typical value of $v = 2{\cdot}2$ km/s, $T_0 \sim \frac{W}{2\beta}$, and $\beta \sim 3{\cdot}0$ km/s. Here, it may be assumed that for typical strike slip faulting in California, the dislocation grows more or less as a circular dislocation up to $r \leq W/2$. When the size of W has been reached, it is assumed that the fault surface grows in terms of L only. Thus, $\omega\tau$ is approximated in eqn (13) by

$$\omega\tau \approx \frac{2\pi}{T}\left(\frac{L}{2{\cdot}2} + \frac{W}{6}\right) \tag{14}$$

Far-field displacements

As the observation point moves away from the source, the permanent offset (d_p) goes to zero and the ground displacement, d_{FF}, experiences only a 'transient pulse' which could be characterized by the Brune's[4] pulse,

$$d_{FF}(t) \approx \frac{r}{R} \frac{\sigma\beta}{\mu} t' e^{-\alpha t'}, \quad t' \geq 0 \tag{15}$$

where $t' = t - R/\beta$ (r is the source dimension, $\sigma =$ Brune's effective stress drop, $\beta =$ shear wave velocity, $R =$ source to station distance, and $\mu =$ rigidity). The Fourier amplitude spectrum of d_{FF} in eqn (15) is

$$\Omega_{FF}(\omega) \approx \frac{r}{R} \frac{\sigma\beta}{\mu} \frac{1}{\omega^2 + \alpha^2} \tag{16}$$

and the strong motion acceleration spectrum is

$$FS_{FF}(\omega) \approx \frac{r}{R} \frac{\sigma\beta}{\mu} \frac{1}{1 + \left(\frac{\alpha}{\omega}\right)^2} \tag{17}$$

Since[4] $\alpha \approx 2{\cdot}34\beta/r$, and assuming that $r \sim L/2$ ($r \sim W/2$), for $\beta \approx 3$ km/s, $\alpha/\omega \sim 2{\cdot}23T/L$. As $T \to \infty$, eqn (17) implies that $FS_{FF}(T) \sim 1/T^2$. Also, since[8]

$$\Omega_{\substack{FF \\ \omega \to 0}}(\omega) \to M_0(4\pi\rho R\beta^3)^{-1} \tag{18}$$

$$FS_{\substack{FF \\ \omega \to 0}}(T) \to \frac{\pi M_0}{\rho R\beta^3 T^2} \tag{19}$$

where $\rho = \mu/\beta^2$ and M_0 is the seismic moment defined by

$$M_0 = \mu\bar{u}A \tag{20}$$

$\bar{u}$ is the dislocation amplitude ($\bar{u} \sim 2\bar{d}$) averaged over the fault surface A.

Using the Haskell's[6] representation in the far-field for

S waves, it is possible to compute the Fourier amplitude spectra of the ground displacement, if the dislocation function is specified on the fault surface. Assuming that this dislocation grows linearly during time T_0, until the final dislocation amplitude is reached, and that this dislocation propagates with constant velocity v along the fault of length L, it can be shown that

$$|\Omega_{FF}| \sim \left| \frac{\sin \frac{\omega L}{2v}}{\frac{\omega L}{2v}} \right| \cdot \left| \frac{\sin \frac{\omega T_0}{2}}{\frac{\omega T_0}{2}} \right| \tag{21}$$

Equation (21) is characterized by two corner frequencies, one, f_1, associated with the duration of faulting (L/v) and the other, f_2, with the duration of the dislocation rise time T_0. As $\omega \to \infty$, like eqn (16), eqn (21) implies $\Omega_{FF} \sim 1/\omega^2$.

If one assumes a dislocation buildup of the form $1 - \exp(-t/T_0)$, for $t > 0$,

$$|\Omega_{FF}| \sim \frac{\sin \frac{\omega L}{2v}}{\frac{\omega L}{2v}} \cdot \frac{1}{(1+\omega^2 T_0^2)^{1/2}} \tag{22}$$

If it is assumed that the duration of the slip is controlled by the narrow dimension of the fault W, then the displacement rise time is $T_0 \sim W/2v$. Assuming that this time should roughly correspond to 90% of the maximum dislocation[52] gives $2{\cdot}3T_0 = W/2v$ and the second corner frequency

$$\omega_2 = 4{\cdot}6v/W \tag{23}$$

For $v \approx 3$ km/s, $f_2 = 2{\cdot}2/W$. The other corner frequency, $\omega_1 \approx 2\pi v/L$, depends on the duration of faulting L/v.

Guided by the above results, the author chose to approximate the far field displacement spectra Ω_{FF} by

$$\Omega_{FF}(T) = C_s \frac{1}{\left[1 + \left(\frac{W}{2{\cdot}2T}\right)^2\right]^{1/2}} \cdot \frac{1}{1+\frac{\tau}{T}} \tag{24}$$

where the 'constant' C_s can be computed from

$$C_s = FS_{FF}(\omega_c)\omega_c^{-2}\left[1 + \left(\frac{W}{2{\cdot}2T_c}\right)^2\right]^{1/2}\left(1+\frac{\tau}{T_c}\right) \tag{25}$$

with $\omega_c = 2\pi/T_c$ and $T_c \equiv T(N_c)$ (see Table 2), and where $FS_{FF}(\omega_c)$ is set equal to the spectral amplitude computed from eqn (1) or its equivalent for one of the four models (G4*RM*). Via $FS_{FF}(\omega_c)$, C_s depends on magnitude, distance and local site conditions, and is therefore evaluated at the same epicentral distance R which is used to compute $FS(T)$ from eqn (1). Since eqn (18) requires that $FS(T)T^2 \sim 1/R$, C_s should also be proportional to $1/R$. This condition is satisfied approximately for $\sim 50 < R < 150$ km.

The empirical estimates of the spectral amplitudes in eqn (1), for small Δ, first decrease with T approaching T_c and then begin to curve up near $T = T_c$ and for $T > T_c$. In part, this is due to the decreasing signal to noise ratio in the recorded accelerograms,[32,33] but it is also believed that it results from the gradual transition of the empirically computed spectral amplitudes to the slopes which are analogous to those defined by eqn (13), for $\omega < 2\pi/T(N_c)$. In this work, the author first chose N_c so that $T(N_c)$ is near such turning points. Then, by trial and error, he selected the final values of N_c (see Table 2) to obtain the 'best fit' with various data and known constraints. In the end, for the far-field strong motion amplitudes, eqn (1) was used to predict $FS(T)$ for $T < T(N_c)$ and $\omega^2\Omega_{FF}$, with Ω_{FF} given by eqn (24), and C_s computed from eqn (25).

Since 1970 many authors considered only one corner frequency ($\alpha = 2{\cdot}34\beta/v$) in their interpretation of the far field shear wave spectra. More recent observations of intermediate and large earthquakes show that at least two corner frequencies (f_1 and f_2) should be used to describe the body wave spectra. For intermediate and small earthquakes f_1 and f_2 become comparable to and higher than 1 Hz, and for $M < 3$, the low-pass filtering effects of Q then make it difficult to observe f_1 and f_2, and to distinguish them from the Brune's single corner frequency α (see also Fig. 7 (later)).

Transition between near-field and far-field spectra

To provide a continuous transition between $\Omega_{NF}(\omega)$ and $\Omega_{FF}(\omega)$ and to complete a representation for use in engineering applications, the author uses the results of Jovanovich *et al.*[53,54] They show that the error in representing the static displacement field by a point source is typically less than 5% at distances greater than $4L$, where L is the source length. The distance S_1, between the station and the 'top' of the vertical fault with 'dimension' S (see eqns (3) and (4), and Gusev[3]) and at depth H is defined as

$$S_1 = \begin{cases} [R^2 + (H-S)^2]^{1/2}, & H \geq S \\ R, & H < S \end{cases} \tag{26}$$

Here, $S = 0{\cdot}01 \times 10^{0{\cdot}5M}$ when $S \leq 30$ km, and $S = 30$ km for larger events, and then $FS_{NF}(T)$ and $FS_{FF}(T)$ are combined as follows

$$FS(T) = FS_{NF}(T)\, e^{-\left(\frac{3S_1}{4S}\right)} + FS_{FF}(T)\left(1 - e^{-\left(\frac{3S_1}{4S}\right)}\right), \quad T > T(N_c) \tag{27}$$

In the above expression, 3/4 is used to scale S_1/S so that when $S_1/S = 4$, the exponent is equal to 3 (so that $e^{-3} \sim 0{\cdot}05$), in agreement with the recommendation of Jovanovich *et al.*[53,54] For $T < T(N_c)$ (see Table 2), equations of the type illustrated by eqn (1) are used, depending on which of the G4*RM* is used.

For $f < f_{co}(= 1/T(N_c))$, the heavy solid lines in Fig. 1

show $FS(T)$ computed from eqn (27). For $R = 10$ km, $H = 0$ and $M = 4$ (bottom heavy solid line), since S_1 and Δ are both greater than $4S$, $FS_{FF}(T)$ contributes mainly to $FS(T)$, and so $FS(T) \sim 1/T^2$. For $M > 7$, S_1 and Δ are smaller than $4S$, and the amplitudes of $FS(T)$ shown in Fig. 1 are dominated by the flat portion of $FS(T) \sim d_p/\tau$ (see eqn (13)), for T near and longer than $1/f_1$. For $M = 5$ and 6, the spectra, $FS(T)$, display a progressively changing slope for $f < f_1$. With increasing M (increasing S), this slope decreases from -2 towards 0, as M goes from 4 to 7 and 8, in the period range shown in Fig. 1.

COMPARISON OF VARIOUS SOURCE PARAMETERS WITH PREVIOUS DATA AND INTERPRETATION

The selection of $T(N_c)$, where the empirical (eqn (1)) and extrapolation equations (eqn (27)) meet, and the assumed dependence of W and L on magnitude define the near-field and the far-field long period Fourier spectral amplitudes of strong motion as outlined in the above eqns (13) and (24). These equations, in turn, imply a number of other source characteristics, which can be compared with other independent estimates and with other observations. In the following are shown some of these comparisons, to test the suitability of the chosen functional forms of the eqns (13) and (24), of their scaling parameters, and of the overall extrapolation method.

Permanent displacements

By computing Fourier spectrum amplitudes (in the near field) for $T \to \infty$, it is possible to evaluate the average dislocation $\bar{u}$ (in cm) implied by the G4*RM* models and by the choices for L and W (Table 5 (later); L and W will be discussed later). For this, we first equate eqns (1) and (13) at $\omega_c = 2\pi/T_c$, assuming that $\omega\tau$ is given by eqn (14) (L and W will be computed from eqns (29) and (30) for given M) and compute d_p. Then, letting $\omega \to 0$ in eqn (11), and multiplying d_p by 2 we obtain $\bar{u}$. The result can be compared with other independent estimates of $\bar{u}$. For continuity with the previous studies,[22] and to focus on earthquakes which contributed to this data base,[44,45,55] the data on $\bar{u}$, as shown in Fig. 2 are used. The shaded regions correspond to $\bar{u}$ estimated from the G4*RM*, for probabilities of exceedance ($p(\epsilon, T)$ in eqn (7)) equal to 0·1, 0·5 and 0·9, and for the fault model 3 (Table 5 (later)) as an example. It is seen that the trends of $\bar{u}$ associated with the GR*RM* (as $T \to \infty$) are in excellent agreement with the estimates of $\bar{u}$ using strong motion data, but are larger than the estimates of Thatcher and Hanks,[56] which are based on distant seismological recordings.

Analysis of the accuracy of $\bar{u}$ will reveal that considerable simplifications are required to obtain the data shown in Fig. 2. Likewise, the above extrapolation of $FS(T \to \infty)$, using eqn (13), to evaluate $FS(T)$ for $T > T(N_c)$ depends on the proper choice of $\omega\tau$ versus M (i.e. choice L and W versus M) and on the selection of

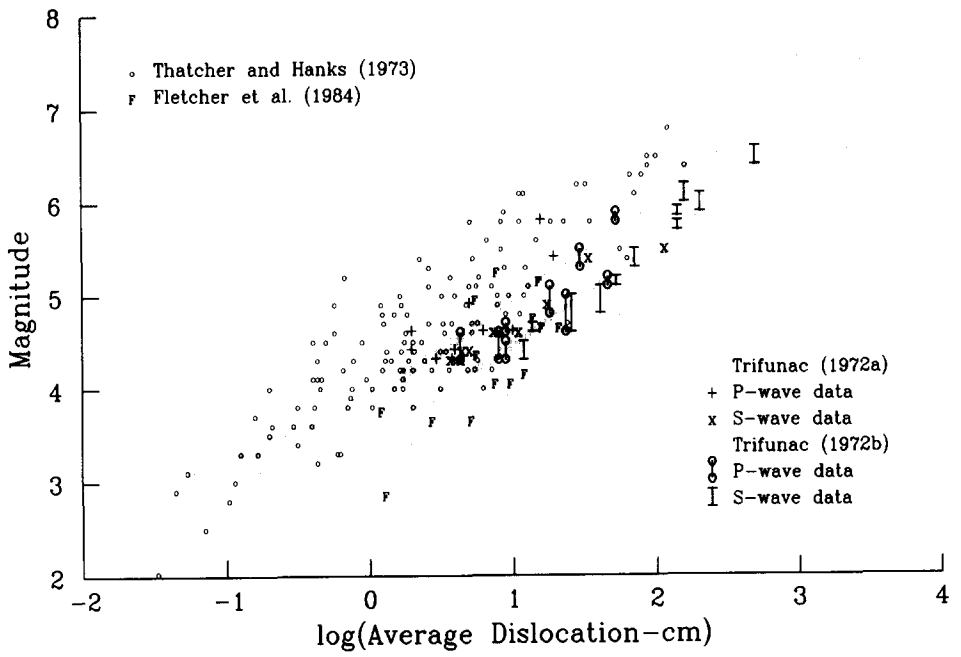

Fig. 2. Comparison of seismically measured (Thatcher & Hanks,[56] Trifunac,[44,45] Fletcher *et al.*[55]) and calculated (using G4*RM*) average dislocation, $\bar{u}$, versus magnitude, M. The three shaded bands show the range of $\bar{u}$ for probabilities of exceedance equal to 0·1, 0·5 and 0·9. The variations within each band show the fluctuations and differences among the four scaling models (1. MAG-SITE, 2. MAG-DEPTH, 3. MAG-SITE-SOIL and 4. MAG-DEPTH-SOIL) and for the fault model 3 representation of L and W (see Table 5).

N_c in $T(N_c)$. Yet, the agreement of the estimated $\bar{u}$ (using eqns (1) and (13) at ω_c), with the independent estimates in Fig. 2 suggests that the empirical spectral amplitudes of $FS(T)$ contain most of the relevant information, up to and including $T = T(N_c)$, to define the average $FS_{NF}(T)$ for $T \gg T(N_c)$.

Comparison of M_0 determined from strong motion accelerograms with other estimates

Equations (21), (23) and (25) result from a simplified consideration of the shear wave spectra only, while $FS(T)$ estimated from eqn (1), via one of the G4*RM*, represent the Fourier amplitudes of the complete strong motion signal including all the waves. In recent work on local magnitude scale[23] computed from strong motion accelerograms, M_L^{SM}, it was found that using the complete time history of strong motion near a source leads to systematically larger estimates, when compared with more distant seismological estimates of M_L. This difference $D(\bar{M}_L^{SM}) = M_L^{SM} - M_p$ (where M_p is the published magnitude), for the strong motion data in the Western USA, is summarized in Table 4. It can be used to adjust the moment M_0^{SM}, computed from eqns (19) and (25), to agree with the distant (say further than 200 km) estimates of the moment M_0

$$\log_{10} M_0 \approx \log_{10} M_L^{SM} - kD(\bar{M}_L^{SM}) \qquad (28)$$

In eqn (28), the factor k is the empirical slope of $\log_{10} M_0$ versus M (e.g. Wyss and Brune[57]), and M_0^{SM} is the seismic moment computed from eqns (18), (24) and (25) using the strong motion data in terms of the G4*RM* ($M_0^{SM} = C_s 4\pi\rho R\beta^3$). The author used $k = 1$ for $M < 4{\cdot}5$, $k = 1{\cdot}25$ for $4{\cdot}5 \le M < 5$, $k = 1{\cdot}5$ for $5 \le M < 7$, and $k = 1{\cdot}3$ for $M \ge 7$, in eqn (28).

Equation (28) can be used then to evaluate M_0 from M_0^{SM}, and to compare it with other independent distant (>200 km) estimates. This is shown in Fig. 3, where the three shaded zones, for probabilities of exceedance equal to 0·1, 0·5 and 0·9, show $\log_{10} M_0$ versus magnitude. In

Table 4.[a] $D(\bar{M}_L^{SM}) = \bar{M}_L^{SM\,b} - M_p{}^c$ **versus** M_p

M_p	$D(\bar{M}_L^{SM})$	M_p	$D(\bar{M}_L^{SM})$
3·1	1·30 (1·70)[d]	6·4	0·27 (0·29)
3·5	1·24 (1·60)	6·8	0·03
4·0	1·15 (1·45)	7·0	−0·11
4·5	1·05 (1·26)	7·4	−0·40
5·0	0·9 (1·05)	7·7	−0·63
5·5	0·72 (0·81)	8·0	−0·87
6·0	0·47 (0·53)		

[a] From Trifunac.[23]
[b] Local magnitude estimated from computed response of Wood–Anderson seismograph excited by the recorded strong motion acceleration.
[c] The published earthquake magnitude typically corresponding to M_L for $M_p \le 6{\cdot}5$.
[d] $D(\bar{M}_L^{SM})$ as used in this study is based on the subjective manual fit of the data[24] in the low magnitude range, typically $M < 5$. The values shown inside brackets represent the smooth parabolic fit to all data as in Trifunac.[23]

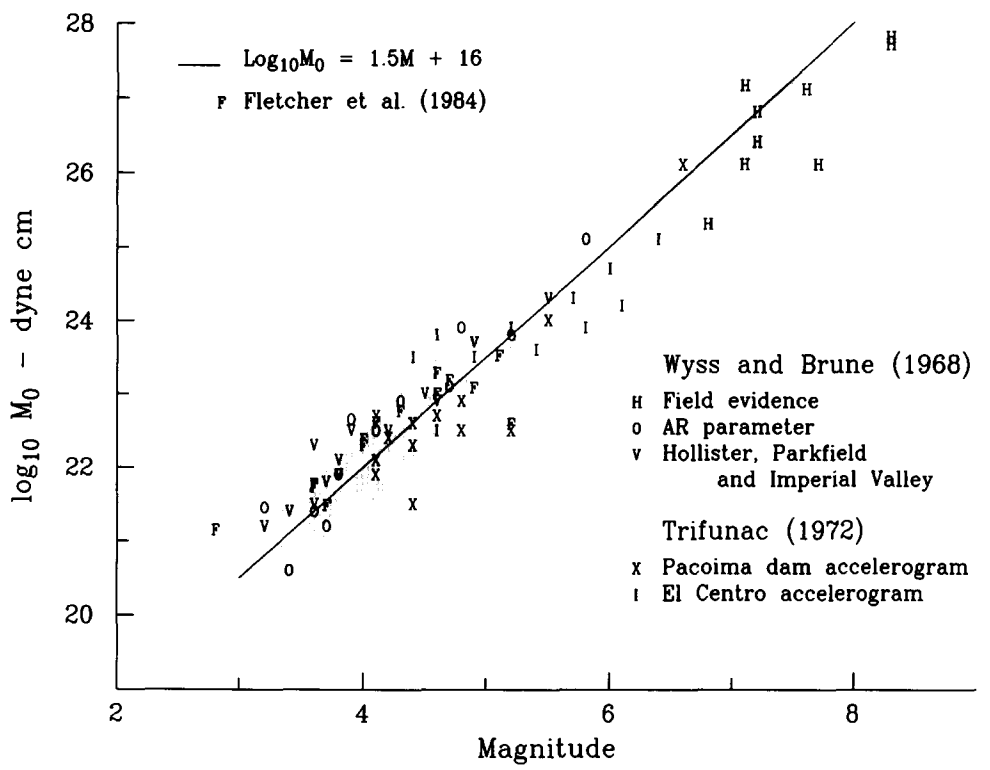

Fig. 3. M_0 versus M for selected teleseismic (Wyss & Brune[57]) and strong motion estimates (Fletcher *et al.*,[55] and Trifunac,[44,45]) of M_0. The three shaded regions show the range of estimates for three probabilities of exceedance (0·1, 0·5 and 0·9), computed for the G4*RM*.

this calculation, the author used a variable value of $\mu\beta$ as follows. The typical shear wave velocity in the source region was assumed to increase linearly from 0·5 km/s at the surface to 4 km/s at a depth of 10 km. The material density was also assumed to increase linearly, from 2 g/cm^2 at the surface to 3 g/cm^3 at a depth of 10 km. The fault surface was assumed to be vertical with the lower long edge (along L) at $H = 10$ km, and with the top edge at $H - W$ (km). μ and ρ were calculated at depth $H - W/2$, for W specified by one of the four fault models (see Fig. 4 and Table 5). The resulting $\mu\beta$ ranged from $4{\cdot}7 \times 10^{16}$ dyne/cm/s (for $M = 8$) to $18{\cdot}12 \times 10^{16}$ dyne/cm/s (for $M = 3$). The straight line given by $\log_{10} M_0 = 1{\cdot}5M_0 + 16$, and selected data on field and seismic estimates of the moment M_0 using body wave spectra and using strong motion data are also shown in Fig. 3. It is seen that the agreement between our estimates based on eqn (18) and the above procedure, and the results from the previous studies is good.

A trend of departure of the data points on $\log_{10} M_0$ versus magnitude from a straight line (with the slope $k \sim 1{\cdot}5$) near $M = 4$ has been observed for several data sets in California and elsewhere.[58] Its explanation has been sought in terms of different stress drops for some $M < 4$ events, resulting in systematically higher corner frequencies.[59,60] Also this change occurs for events whose corner frequencies are close to the corner frequency of the Wood–Anderson seismometer.[12,55] The physical considerations of the source mechanism, for most earthquakes (with rupture time longer than 5–10 s, and with rise time shorter than ~5 s), lead to $\log_{10} M_0 \sim 1{\cdot}5M$. For small earthquakes (with magnitudes less than ~4–5), having smaller dimensions and shorter rise time,[61,62] $\log_{10} M_0 \sim M$.

Using the equation $\log_{10} E_S = 1.5M_s + 11{\cdot}8$ to relate the surface wave magnitude, M_S, and the total energy of seismic waves,[63] E_S, and the equation $E_S = \eta\bar{\sigma}M_0/\mu$, where $\eta\bar{\sigma}$ is the apparent stress, leads to

$$\log_{10} M_0 = 1{\cdot}5M_S + 11{\cdot}8 - \log_{10}\frac{\eta\bar{\sigma}}{\mu}$$

For $\eta\bar{\sigma} = 10$ bars, and equating M_S with M_L for magnitudes smaller than about 7, gives $\log_{10} M_0 = 1{\cdot}5M + 16{\cdot}1$. In Fig. 3, showing the trends for the G4*RM* and the four fault models (Table 5), it is seen that the average trend of $\log_{10} M_0$ versus M is close to $\eta\bar{\sigma} = 10$–20 bars.

For completeness of this discussion, note that since $M_0 = \mu\bar{u}A$ and $A \approx ac \times 10^{(b+d)M}$ (see Table 5), and $\bar{u} = C_0^*\sigma W/\mu$ (Table 3), one can write $\log_{10} M_0 = \log_{10}(C_0^*\sigma ac^2) + (b + 2d)M$. For $M < M_*$, $b + 2d \sim 1{\cdot}5$, and for $M > M_*$, $b + 2d \sim 1{\cdot}1$, Also, for $M \leq 4$, $\log_{10}\sigma \sim -0{\cdot}75 + \frac{M}{2}$, for $4 < M < 6$, $\log_{10}\sigma \sim \frac{1}{3}M$, and for $7 < M < 8$, $\log_{10}\sigma \sim 1{\cdot}4 + (1/9)M$. Thus, when $M < 4$, the G4*RM* imply $\log_{10} M_0 \sim 2M$, for $4 < M < 6$ $\log_{10} M_0 \sim 1{\cdot}5M$, and for $M > 7$, $\log_{10} M_0 \sim 1{\cdot}3M$. However, for $M < 4$, f_1 and f_2 become comparable to, and for small M, exceed f_p (Fig. 1), and so our estimates of W and L (via f_1 and f_2) may not be reliable, and are probably too large for this magnitude range. The estimates of $\log_{10} M_0$ larger than the linear trend implied by $1{\cdot}5M + 16$ in Fig. 3, for $M < 4$, may not be real, but merely a consequence of the natural low-pass filtering of the spectra of recorded motions by low Q. Many small magnitude strong

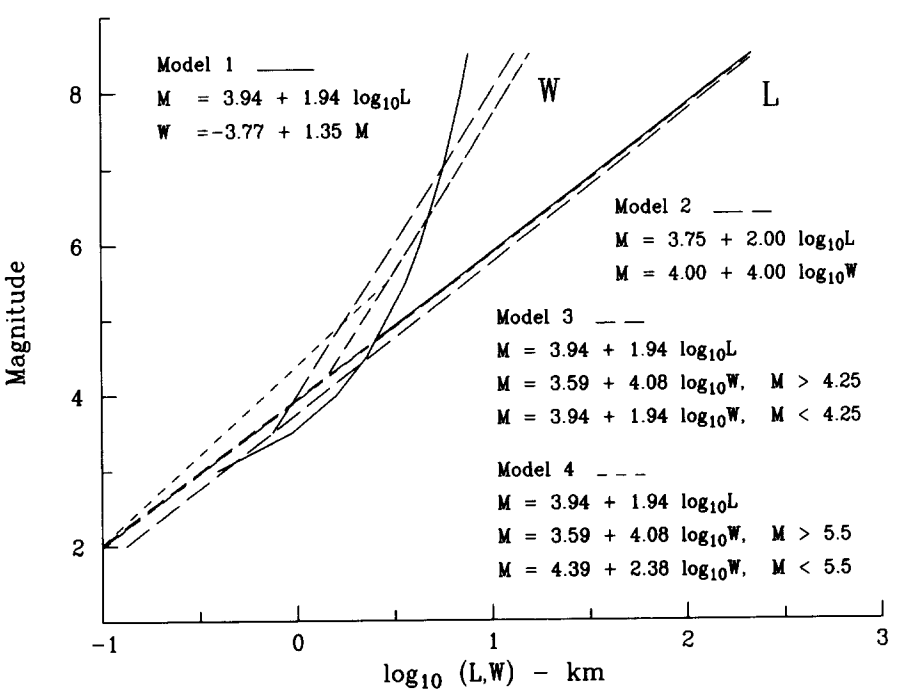

Fig. 4. Fault length (L) and width (W) versus earthquake magnitude for models 1, 2, 3 and 4.

Table 5.[a] Coefficients a and b in $L_{min} = a \times 10^{bM}$ and c and d in $W = c \times 10^{dM}$

Fault length L_{min} (km)			Fault width W (km)		
Model[b]	a	b			
1	0·009 31	0·515	$W = \begin{cases} -3{\cdot}77 + 1{\cdot}347M & M > 3.1 \\ 0{\cdot}131M & M < 3{\cdot}1 \end{cases}$		
			c	d	
2	0·0133	0·50	0·1	0·25	$M > 3.5$
			$W = L$	for	$M < 3.5$
3	0·009 31	0·515	0·132	0·245	$M > 4{\cdot}25$
			$W = L$	for	$M < 4{\cdot}25$
4	0·009 31	0·515	0·132	0·245	$M > 5{\cdot}5$
			0·0145	0·419	$M < 5{\cdot}5$

[a] In the text these magnitudes are designated by M_*.
[b] Fault models 1–4 have been chosen to illustrate the plausible variations in W and L (allowed by the data), and the consequences of these variations on other characteristics of the models.

motion accelerograms ($M < 3{\cdot}5$) must be recorded near or at the source (e.g. $\Delta < 10$ km) to interpret the trends of $\log_{10} M_0$, f_1 and f_2 versus M in this magnitude range.

Equations (19) and (25) imply that $C_s \sim 1/R$, while the amplitudes of FS_{FF}, computed from $FS(T)$ at $T(N_c)$, attenuate like $\Delta^{\mathcal{A}_0(T)}$ (see eqn (2)). However, C_s is computed from eqn (25) at different cut-off periods $T(N_c)$, and so it depends on magnitude directly through $FS(T)$ and indirectly through W and L (i.e. τ). To verify that $C_s \sim 1/R$ and that eqn (19) indeed results in M_0 which is independent of R, the author computed $\log_{10} M_0$ versus M for R in the range from 0 to 200 km. For $50 < R < 150$ km, the results were insensitive to R. For the cases considered, near $R = 200$ km, eqn (28) underestimated $\log_{10} M_0$ by about 0·2. For $R < 50$ km, $FS(T)$ in eqn (1) begins to be sensitive to the near-field effects, and eqn (28) ceases to apply.

Comparison with other estimates of L and W

For intra-plate earthquakes, the estimates of the fault width, W, suggest growth of $\log_{10} W$ versus magnitude, up to $W \approx 5$–10 km and for $M \approx 6$. For larger magnitude events, W seems to become less dependent on magnitude.[40–43,46–48,64] Correlations of the fault

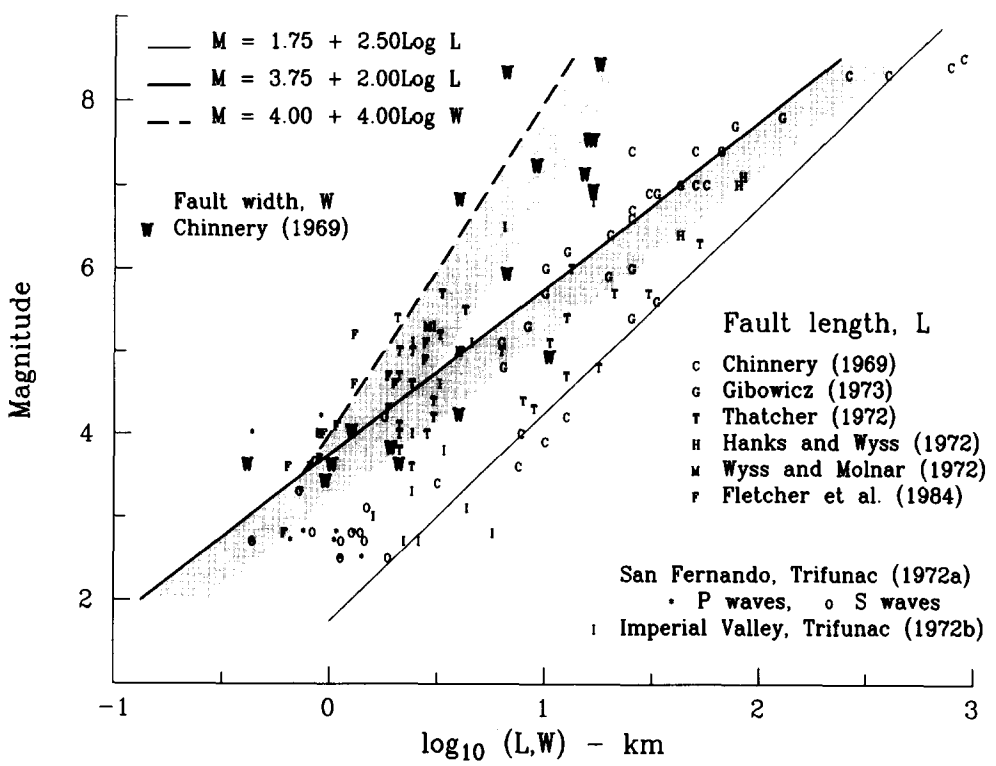

Fig. 5. Field and instrumental estimates of the fault width (W) and the fault length (L) versus magnitude M.[30,44,45,55,64–67] L_{min} and W_{min} (e.g. for Model 2), assuming unilateral propagation of the dislocation, are shown by the heavy continuous (L) and broken lines (W). Symmetrically bilateral faults would result in two times larger fault dimensions. All other faulting falls between these two estimates and is shown by the shaded zones in this figure.

length, L, and magnitude show large fluctuations (for $3 \leq M \leq 8$), but most estimates tend to fall between

$$L_{\min} \approx a \times 10^{bM} \tag{29a}$$

and

$$L_{\max} \approx 0{\cdot}20 \times 10^{0{\cdot}40M} \tag{29b}$$

where L is measured in kilometers.[53,54]

The fault width W can be approximated by

$$W = c \times 10^{dM} \tag{30a}$$

or by

$$W = e + fM \tag{30b}$$

Table 5 presents the coefficients a–f for the four cases (referred to as fault models 1–4) used as examples in this study (Fig. 4). As will be seen from the following, it is remarkable that both L and W can be approximated with so simple functional forms and for such a broad range of magnitudes. Furthermore, various constraints on the spectral amplitudes limit the permissible fluctuations of L and W to a relatively narrow range, making fault models 1–4 very similar, and thus controlling the possible range of the coefficients a, b, c, d, e and f, which were chosen here by trial and error.

In eqn (14), $L = a \times 10^{bM}$ was chosen, which corresponds to $L_{\min}$ already mentioned in eqn (29) and for a and b as given in Table 5. Also $W_{\min} = W$ was chosen (as in eqn (30)). As will be clear from the following, $L_{\min}$ and $W_{\min}$ correspond to the smallest fault dimensions for unilateral faulting. For bilateral (symmetric), faulting $L \sim 2L_{\min}$ and $W \sim 2W_{\min}$.

For small intra-plate sources (e.g. $M < 4$–5), the fault length, L, and width, W, are about the same. For larger earthquakes, the fault continues to grow mainly through L, while W may only continue to increase slowly until it reaches the width of the seismogenic zone. A range of models describing W in terms of M has been considered in this paper. This analysis showed that the permissible variations of W versus magnitude are controlled well by the available data and suggested typical models with $W = L$ for $M < M_*$ and $W = c \times 10^{dM}$ for $M > M_*$ (Table 5). This dependence of L and W on magnitude is also in good agreement with the data on the field estimates of L and W (Fig. 5) and with the data on the second corner frequency, f_2, which is seen in the far-field spectra of shear waves,[20] and can be approximated by $2{\cdot}2/W$ (eqn (23)).

In Fig. 5, the shaded zone to the right of $L_{\min}$ and $W_{\min}$ (see eqns (29a) and (30)) outlines the range $L_{\min} < L < 2L_{\min}$ and $W_{\min} < W < 2W_{\min}$, in this example for the fault model 2 (Table 5). In

$$\tau = \frac{L}{v} + \frac{W}{2\beta} \quad \text{(assuming that } L \gg W\text{)}$$

the duration, τ, is defined by a dislocation propagating unilaterally $L_{\min}$ km from the focus at one end of the fault, towards the other end of the fault. Since it is the duration of faulting which is constrained by $\omega\tau$ and is fitted to the strong motion spectral amplitudes, it is seen that, for bilateral faulting, our scaling implies that the fault length $L = 2L_{\min}$. Thus, all field observations of fault length falling between $L_{\min}$ and $2L_{\min}$ would be in agreement with our interpretation of near-field strong motion data, assuming some distribution of events in the range between unilateral and bilateral faulting. Detailed comparison of our estimates (exemplified by the fault models 1–4) with field and seismological estimates of fault length and width[53,54] (Fig. 5) indicates good agreement.

Corner frequencies $f_1 = (\frac{L}{2{\cdot}2} + \frac{W}{6})^{-1}$ and $f_2 = \frac{2{\cdot}2}{W}$

Figure 6 shows $\log_{10} f_1^2 M_0$ and $\log_{10} f_2^2 M_0$ plotted versus $\log_{10} M_0$ for the four fault models. These can be approximated by the linear trends

$$\log_{10} f_1^2 M_0 = 15{\cdot}1 + \frac{1}{3}\log_{10} M_0 \tag{31}$$

$$\log_{10} f_2^2 M_0 = 7{\cdot}7 + \frac{2}{3}\log_{10} M_0, \quad \log_{10} M_0 > 23 \tag{32}$$

For small M_0, f_1 and f_2 are nearly the same. Near $\log_{10} M_0 \sim 20$, f_2 slowly becomes larger than f_1, and

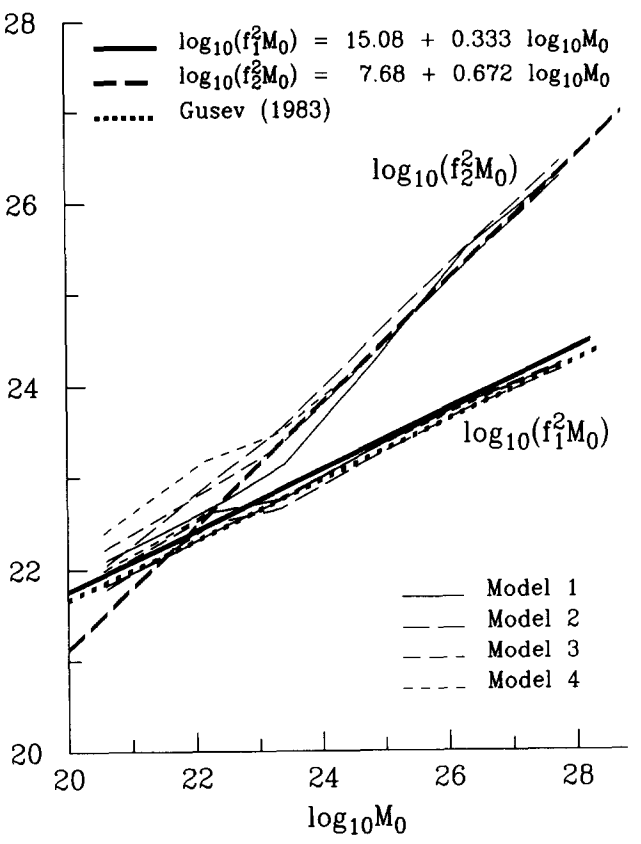

Fig. 6. $\text{Log}_{10} f_1^2 M_0$ and $\log_{10} f_2^2 M_0$ versus $\log_{10} M_0$.

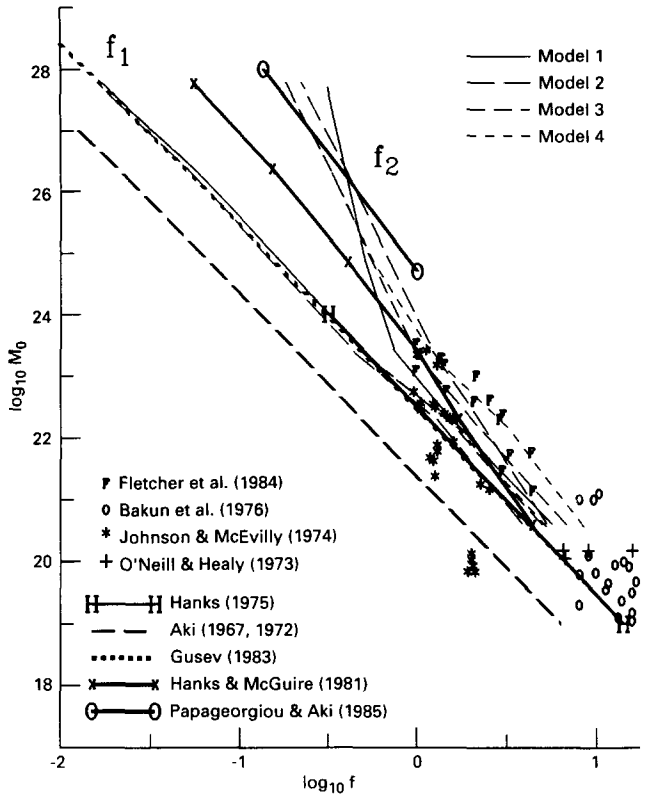

Fig. 7. $\log_{10} M_0$ versus $\log_{10} f_1$ (after Chouet *et al.*[70]), and $\log_{10} f_2$ (using data from Refs 3, 15–17, 55, 60, 68, 69, 71, 72).

after a transition region, $20 < \log_{10} M_0 < 23$, $\log_{10} f_2^2 M_0$ attains its own trend as in eqn (32). The trend of $\log_{10} f_1^2 M_0$ as used by Gusev[3] is also shown, and agrees well with our results.

Figure 7 compares our results on $\log_{10} M_0$ versus $\log_{10} f_1$ and $\log_{10} f_2$ with the analysis of Chouet *et al.*[70] It is seen that our curves for the extrapolation models 1–4 for f_2 and f_1 agree well with the observed corner frequencies, with the corresponding trends for f_1 of Hanks[71] and Gusev,[3] and with f_2 from Papageorgiou and Aki.[15] For $\log_{10} M_0 < 19$, the observed corner frequencies in the paper by Chouet *et al.*[70] cease to increase with frequency, apparently due to the low-pass filtering effects of the attenuation. The corner frequency of Hanks and McGuire[72] is close to our $\log_{10} f_2$ for $\log_{10} M_0 < 25$, and then is roughly in the middle between our $\log_{10} f_1$ and $\log_{10} f_2$ for $\log_{10} M_0 > 25$.

Another way of combining the data on f_1, f_2 and M_0 is to plot $\log_{10} f^2 M_0$ versus f. Figure 8 shows an example (fault model 1 in Table 5) of our estimates of $f_1^2 M_0$ and $f_2^2 M_0$ versus f, and compares those with the data used by Papageorgiou.[20] In making this comparison, no attempt is made to establish what is the physical meaning of f_2. It is only recognized that such a corner frequency is observed by some investigators[14,73] and that it is not difficult to associate it with $f_2 \sim 2{\cdot}2/W$. The fault models 2, 3 and 4 result in very similar trends, and agree equally well with the data on f_1, f_2 and M_0.

Characteristic source durations T_0 and τ

Assuming that the time rate of growth of the dislocation amplitudes is proportional to the effective stress drop,[4] and that the multiple events are excluded from this consideration, the dislocation rise time T_0 (Table 6) can be estimated from

$$T_0 \sim \frac{\bar{u}\mu}{\sigma\beta} \tag{33}$$

This should also be related to the time it takes for the dislocation to propagate through the full fault width W, and since $W \sim 1/f_2$, $f_2 T_0$ should be nearly constant, perhaps only slowly changing with magnitude (i.e. the fault geometry via C_0^*; see Tables 3 and 6). Thus, in terms of the overall source duration characteristics (integrating over the high frequency pulses that may result from asperities and fault barriers), T_0 might be viewed as the shortest overall characteristic duration of the source. On the other hand, $\tau = \frac{L}{v} + T_0$ can be viewed as the longest characteristic source duration, where v can be chosen so that it incorporates the delays between the multiple rupture events, when those do occur in the corresponding frequency and wave length domains.

Figure 9 shows the trends of the durations T_0 and $\tau = 1/f_1$ versus seismic moment M_0 for the G4*RM* studied here. For comparison, it shows also the data on source duration compiled by Somerville *et al.*[74] Their source durations were estimated from the duration of triangular or trapezoidal source functions, which provided the best fit to the teleseismic long and short period body waves. Their data contain 22 events which were recorded in California between 1933 and 1983 and which coincide with most of the events contributing to our strong motion data base used in this work. The method of Somerville *et al.*[74] should give reasonable estimates of source duration for simple events (corresponding to T_0), but it will underestimate the source duration for multiple rupture or multiple plane events. This seems to be confirmed in Fig. 9 where most points fall around T_0 and between T_0 and $\tau = 1/f_1$, but in most cases do not reach τ.

Fault area

The fault area, A, is directly related to the estimates of f_1 and f_2, since $W \sim v/f_2$ and $L \sim v/[f_1(1 + \frac{W}{2{\cdot}7L})]$, giving

$$A = [v^2/(f_1 f_2)]\left(1 + \frac{W}{2{\cdot}7L}\right)^{-1} \tag{34}$$

Using the approximations for $L = a10^{bM}$ and $W = c10^{dM}$ gives

$$A = ac10^{(b+d)M} \tag{35}$$

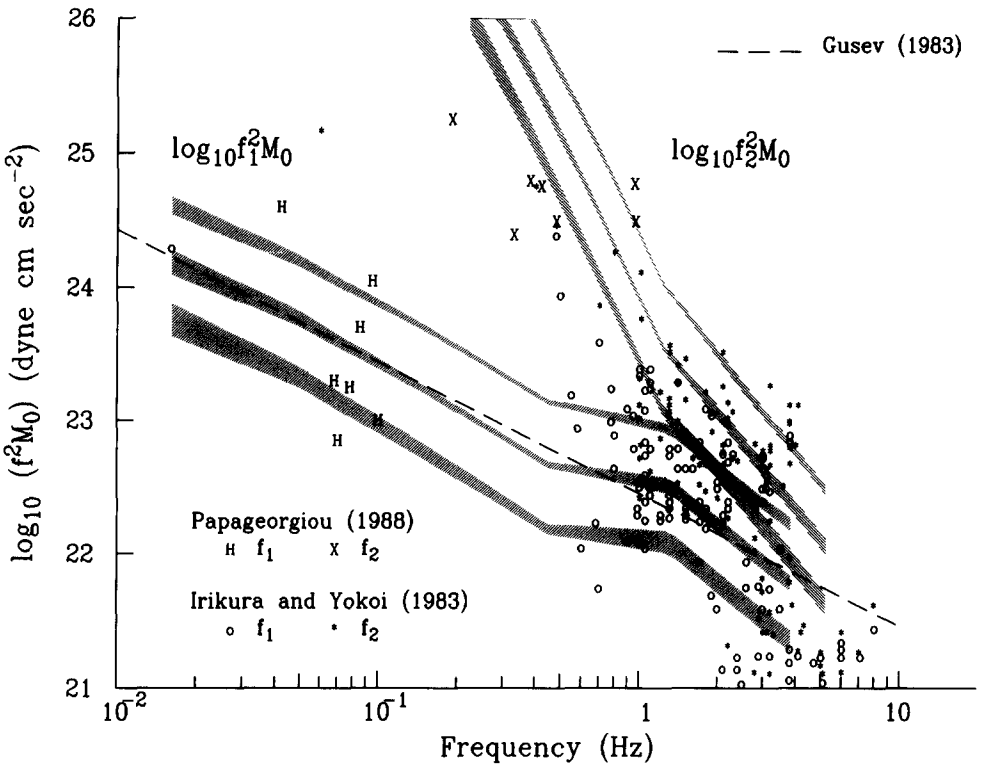

Fig. 8. $\text{Log}_{10} f^2 M_0$ versus f with data from Papageorgiou[20] and Model 1 (Table 5). The three shaded bands correspond to probabilities of exceedance equal to 0·1, 0·5 and 0·9 and for the G4*RM*.

Then, from Table 5, $ac \sim 0{\cdot}001$–$0{\cdot}0017$ and $(b+d) \sim 0{\cdot}74$–$0{\cdot}77$. For large events ($M > M_*$), Table 5 thus implies

$$\log_{10} A \approx \frac{1}{2} \log_{10} M_0 - 11, \quad M_0 > 10^{23} \tag{36}$$

assuming[57] that $\log_{10} M_0 \sim 1{\cdot}45M + 16$, and that $M_0 > 10^{23}$. For $M < M_*$, $ac \sim 0{\cdot}0001$ and $b + d \sim 1$, giving

$$\log_{10} A \approx \frac{2}{3} \log_{10} M_0 - 14{\cdot}8, \quad M_0 < 10^{23} \tag{37}$$

Thus, our four fault models result in the slope of $\log_{10} A$ versus $\log_{10} M_0$ equal to $\sim 2/3$ for $M < M_*$, and to $\sim 1/2$ for $M > M_*$. We note that the equation $\log_{10} M_0 = \frac{3}{2} \log_{10} A + 22{\cdot}25$, for $10^{25} < M_0 < 10^{30}$, used by Purcaru and Berckhemer[75] would be identical to eqn (37) if extrapolated to $M < 10^{25}$. This remarkably constant slope, equal to 2/3, for the entire range $10^{21} < M < 10^{30}$ implies $\log_{10} \mu\bar{u} \sim$ constant.

Table 6. Average rise time T_0^* in seconds and average C_0^*, versus magnitude

M	T_0 (s)[a]	C_0^*
3	0·05	0·4
4	0·31	0·5
5	0·73	0·65
6	1·6	0·85
7	5·4	1·6
8	(26·4)	(1·6)

[a] $\mu/\beta = 0{\cdot}3 \times 10^6$ dyne s/cm^3.

Starting with the definition of seismic moment $M_0 = \mu A \bar{u}$ and representing $\bar{u} \sim C_0^* \frac{W\sigma}{\mu}$ gives

$$\log_{10} A = \log_{10} M_0 - \log_{10} C_0^* W\sigma \tag{38}$$

An advantage of this expression is that it eliminates μ and can be used to test the internal consistency of various estimates when μ is not known. Using averages from the four fault models to compute C_0^* (Table 6), $\overline{\log_{10} W}$ and $\overline{\log_{10} M_0}$, a family of curves representing eqn (38) can be shown in Fig. 10, for $\sigma = 1$, 10, 100 and 1000 bars. More directly, $M_0 = \mu\bar{u}A$ gives

$$\log_{10} A = \log_{10} M_0 - \log_{10} \mu - \log_{10} \bar{u} \tag{39}$$

In eqn (39), $\log_{10} \bar{u}$ can be computed from the long period estimates of spectral amplitudes (eqn (13) and Fig. 2) in the near field, and $\log_{10} M_0$ can be determined from the long period spectra of the far-field motion (eqn (19) and Fig. 3). For the fault model 2 as an example, and for the range of amplitudes computed from the G4*RM*, eqn (39) is shown in Fig. 10 by one of the shaded zones.

For a circular fault and known stress drop, $\log_{10} A$ can also be written as

$$\log_{10} A = \frac{2}{3} \left[\log_{10} M_0 - \log_{10} \frac{16}{7\pi^{3/2}} \sigma \right] \tag{40}$$

Using the average stress drop for the G4*RM* results in the second shaded region shown in Fig. 10. The slope of this equation, 2/3, is consistent with that of eqn (37) for $M < M_*$, while $W \sim L$ for the four fault models

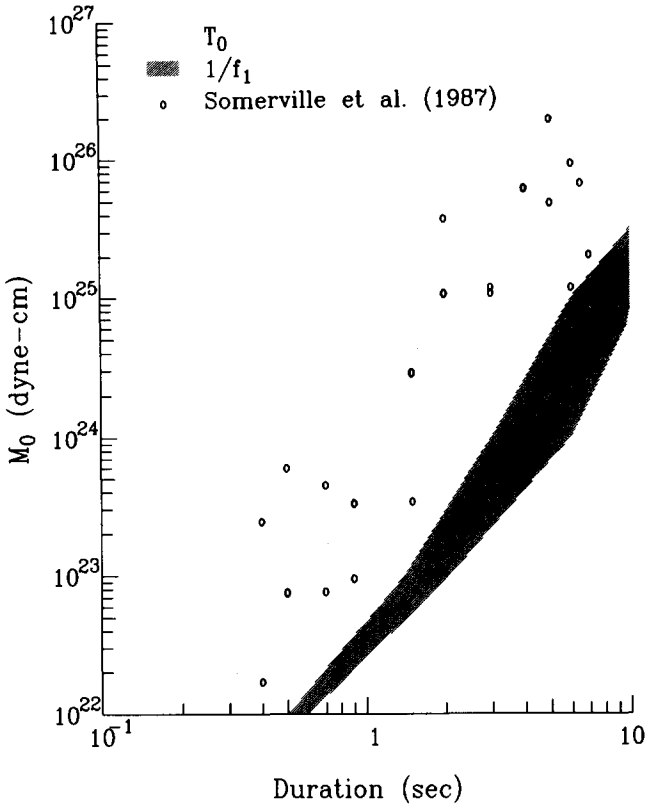

Fig. 9. Comparison of T_0 (the dislocation rise time) and $\tau = 1/f_1$ (the duration of faulting) with teleseismic estimates of source duration.[74] The two gray zones for T_0 and $\tau = 1/f_1$ illustrate the range of values for the four faulting models and for the G4*RM*.

(Table 5). This slope is apparently maintained as long as W and L are approximately the same, even for the largest faults on the subduction zones (e.g. Chile, Alaska; Kanamori and Anderson[61]). In contrast, for the strong motion data in California, where W is limited by the width of the seismogenic zone, for magnitudes near M_*, this slope reduces to 1/2.

Figure 10 also presents examples of $\log_{10} A$, assuming circular dislocation and based on the spectral analysis of strong motion accelerograms.[44,45,55] It is seen that $A = WL$ (the solid continuous curve in Fig. 10) is close to these data, but may overestimate A for $M < 10^{23}$. For $M_0 < 10^{23}$, the data points are also in agreement with $\log_{10} A = 0{\cdot}83 \log_{10} M_0 - 18{\cdot}4$, which is equivalent to $\log_{10} A = 1{\cdot}21 M_s - 5{\cdot}05$ in Båth and Duda.[76]

DISCUSSION AND CONCLUSIONS

The extrapolation equations in this work are based on a simplified description of shear wave spectra. This representation does not evolve from a solution of some specific source slip, but can be thought of as an intuitive collection of relevant parameters and functional relationships based on simple dimensional analyses, which result in a coherent picture of the main features of strong ground motion. The remarkable outcome of this exercise is that the various comparisons of our model with the independent estimates of seismic moment and average dislocation lead to good agreement, and to resolution and scatter which are consistent with many other independent estimates.

The largest uncertainties in our extrapolation exist near $T(N_c)$, where the empirical scaling models approach the recording and processing noise. The tests performed so far suggest that the resulting $FS(T)$ are probably very realistic for $3{\cdot}5 < M < 7$ and for horizontal ground motion. The slopes and amplitudes of empirically computed $FS(T)$ for vertical motions suggest that near $T = T(N_c)$ our empirical models may not be reliable for $M > 6{\cdot}5$. To understand these amplitudes, we need more recorded accelerograms for $M > 7$ and so we must patiently wait for these data to become available.

Extrapolation of $FS(T)$ by eqns (13), (24) and (27), from $T(N_c)$ towards $T \to \infty$ s appears reasonable and agrees favorably with the known trends of the seismic moment, M_0, and of the average dislocation amplitudes, $\bar{u}$, versus earthquake magnitude. Since the corner frequency, $1/\tau$, in the near field ground motion is $\sim v/r$, where v is the dislocation velocity (typically between 2 and 3 km/s), and r is the representative source dimension, it is seen that τ can be larger than $T(N_c)$. This is so assuming that, for the frequencies considered here, the rupture occurs as a 'smooth' process. Many studies have suggested that the fault slips irregularly, with large dislocations distributed at several or at many 'hot' spots, with large dislocation amplitudes, making larger events look like a sequence of smaller events. While this faulting behavior can affect τ appreciably, we do not have, at present, reliable data to identify such behavior in our analysis.

The highly 'local' nature of strong motion recordings, local in the sense of the proximity to the fault (less than say 100 km), and the fact that it is $\bar{u}$ and not the overall source magnitude or moment and the long source dimensions (L) that govern the near-field strong motion amplitudes, all agree with the observed trends of strong motion amplitudes predicted by the G4*RM*.

Numerous further tests and studies of the relationships analogous to eqns (13), (24), (27) and (33) (and of the associated amplitudes, corner frequencies and scaling parameters) are possible. Also the empirical equations exemplified by eqn (1) can be used to investigate the high frequency attenuation and the trends implied by the peaks of spectral amplitudes for frequencies less than 25 Hz. Some of these studies have been completed[50,51] and will be presented in future papers. The picture which emerges from this work is that of detailed internal consistency and agreement with near strong ground motion and distant seismological inferences on one hand, and with the simplified theoretical source representations on the other.

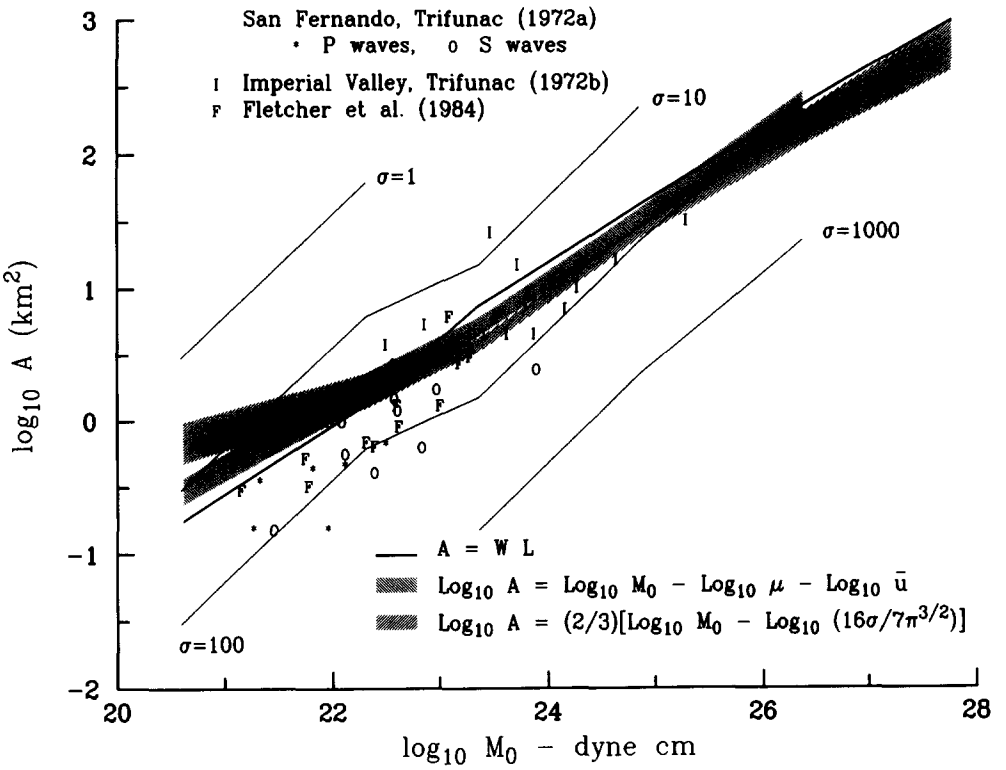

Fig. 10. $\text{Log}_{10} A$ versus $\log_{10} M_0$, comparing the estimates of $\log_{10} A$ using eqns (35), (38) and (39), and selected estimates[44,45,55] based on spectra of strong motion acceleration. $\text{Log}_{10} A_0$ for constant stress drop (σ = 1, 10, 100 and 1000 bars) using eqn (40) are also shown.

REFERENCES

1. Trifunac, M.D. & Lee, V.W. Empirical models for scaling Fourier amplitude spectra of strong ground acceleration in terms of earthquake magnitude, source to station distance, site intensity and recording site conditions, *Int. J. Soil Dynam. Earthqu. Engng.*, 1989, **8**(3), 110–25.
2. Richter, C.F. *Elementary Seismology*, Freeman and Co. S. Francisco, 1958.
3. Gusev, A.A. Descriptive statistical model of earthquake source radiation and its application to an estimation of short-period strong motion, *Geophys. J. R. Astr. Soc.*, 1983, **74**, 787–808.
4. Brune, J.N. Tectonic stress and the spectra of seismic shear waves, *J. Geophys. Res.*, 1970, **75**, 4997–5009.
5. Haskell, N.A. Total energy and energy spectral density of elastic wave radiation from propagating faults, *Bull. Seism. Soc. Amer.*, 1964, **56**, 1811–42.
6. Haskell, N.A. Elastic displacement in the near field of a propagating fault, *Bull. Seism. Soc. Amer.*, 1969, **59**(2), 965–80.
7. Anderson, J.G. Strong motion seismology, In *Contributions in Seismology*, AGU, Washington, DC, 1991.
8. Keilis-Borok, V.I. Investigation of the mechanism of earthquakes, *Sov. Res. Geophys.*, 1960, **4** (Transl. *Tr. Geofiz. Inst.*, **40**), American Geophysical Union Consultants Bureau, New York.
9. Trifunac, M.D. Analysis of strong earthquake ground motion for prediction of response spectra, *Int. J. Earthqu. Engng Struct. Dynam.*, 1973, **2**(1), 59–69.
10. Trifunac, M.D. Dependence of Fourier spectrum amplitudes of recorded strong earthquake accelerations on magnitude, local soil conditions and on depth of sediments, *Int. J. Earthqu. Engng Struct. Dynam.*, 1989, **18**, 999–1016.
11. Trifunac, M.D. Empirical scaling of Fourier spectrum amplitudes of recorded strong earthquake accelerations in terms of magnitude and local soil and geologic conditions, *Earthqu. Engng Engng Vibration*, 1989, **9**(2), 23–44.
12. Boore, D.M. Stochastic simulation of high-frequency ground motions based on seismological models of the radiated spectra, *Bull. Seism. Soc. Amer.*, 1983, **73**(6), 1865–94.
13. Joyner, W.B. A scaling law for the spectra of larger earthquakes, *Bull. Seism. Soc. Amer.*, 1984, **74**(4), 1167–88.
14. Papageorgiou, A.S. & Aki, K. A specific barrier model for the quantitative description of inhomogeneous faulting and the prediction of strong ground motion I. Description of the model, *Bull. Seism. Soc. Amer.*, 1983, **73**(3), 693–722.
15. Papageorgiou, A.S. & Aki, K. Scaling law of far-field spectra based on observed parameters of the specific barrier model, *Pageoph*, 1985, **123**, 353–74.
16. Aki, K. Scaling law of seismic spectrum, *J. Geophys. Res.*, 1967, **72**(4), 1217–31.
17. Aki, K. Scaling law of earthquake source time function, *Geophys. J.*, 1972, **31**, 3–25.
18. Boatwright, J. The seismic radiation from composite models of faulting, *Bull. Seism. Soc. Amer.*, 1988, **78**(2), 489–508.
19. Hanks, T.C. $f_{\max}$, *Bull. Seism. Soc. Amer.*, 1982, **72**(6), 1867–79.
20. Papageorgiou, A.S. On two characteristic frequencies of acceleration spectra: patch corner frequency and $f_{\max}$, *Bull. Seism. Soc. Amer.*, 1988, **78**(2), 509–29.

21. Trifunac, M.D. Preliminary empirical model for scaling Fourier amplitude spectra of strong ground acceleration in terms of earthquake magnitude, source to station distance and recording site conditions, *Bull. Seism. Soc. Amer.*, 1976, **66,** 1343–73.
22. Trifunac, M.D. Preliminary analysis of the peaks of strong earthquake ground motion-dependence of peaks on earthquake magnitude, epicentral distance and the recording site conditions, *Bull. Seism. Soc. Amer.*, 1976, **66,** 189–219.
23. Trifunac, M.D. M_L^{SL}, *Int. J. Soil Dyn. Earthqu. Engng.*, 1991, **10**(1), 17–25.
24. Trifunac, M.D. A note on the difference in magnitudes estimated from strong motion data and from Wood–Anderson seismometer, *Int. J. Soil Dynam. Earthqu. Engng*, 1991, **10**(8), 423–8.
25. Trifunac, M.D. & Lee, V.W. Frequency dependent attenuation of strong earthquake ground motion, *Int. J. Soil Dynam. Earthqu. Engng*, 1990, **9**(1), 3–15.
26. Seed, H.G., Ugas, C. & Lysmer, J. Site dependent spectra for earthquake resistant design, *Bull. Seism. Soc. Amer.*, 1976, **66,** 221–43.
27. Trifunac, M.D. & Lee, V.W. Preliminary empirical model for scaling Fourier amplitude spectra of strong ground acceleration in terms of earthquake magnitude source to station distance, site intensity and recording site conditions, Department of Civil Engineering, Report No. 85-03. University of Southern California, Los Angeles, CA, 1985.
28. Trifunac, M.D. & Lee, V.W. Direct empirical scaling of response spectral amplitudes from various site and earthquake parameters, US Nuclear Regulatory Commission, Report NUREG/CR-4903, Vol 1, 1987.
29. Trifunac, M.D. & Brady, A.G. On the correlation of seismic intensity scales with the peaks of recorded strong ground motion, *Bull. Seism. Soc. Amer.*, 1975, **65,** 139–62.
30. Thatcher, W. Regional variations of seismic source parameters in the Northern Baja California, *J. Geophys. Res.*, 1972, **77,** 1649–65.
31. Amini, A., Lee, V.W. & Trifunac, M.D. Noise in earthquake accelerograms, *ASCE, EMD*, 1982, **108,** 1121–9.
32. Lee, V.W., Amini, A. & Trifunac, M.D. Noise in earthquake accelerograms, *ASCE, EMD*, 1982, **108,** 1121–9.
33. Lee, V.W. & Trifunac, M.D. Automatic digitization and processing of accelerograms using PC, Department of Civil Engineering, Report No. 90-03, University Southern California, Los Angeles, CA.
34. Trifunac, M.D. A note on correction of strong-motion accelerograms for instrument response, *Bull. Seism. Soc. Amer.*, 1972, **62,** 401–9.
35. Trifunac, M.D. & Hudson, D.E. Laboratory evaluation and instrument corrections of strong motion accelerographs, Earthquake Engineering Research Laboratory, EERL 70-04, California Institute of Technology, Pasadena, CA, 1970.
36. Trifunac, M.D. How to model amplification of strong earthquake motions by local soil and geologic site conditions, *Int. J. Earthqu. Engng Struct. Dynam.*, 1990, **19**(6), 833–46.
37. Star, A.T. Slip in a crystal and rupture in a solid due to shear, *Cambr. Phil. Soc. Proc.*, 1928, **24,** 489–500.
38. Knopoff, L. Energy release in earthquakes, *Geophys. J.*, 1958, **1,** 44–52.
39. Keilis-Borok, V.I. On estimation of the displacement in an earthquake source and of source dimensions, *Annali Geofizica*, 1959, **12,** 205–14.
40. Archuleta, R.J. Analysis of near-source static and dynamic measurement from the 1979 Imperial Valley earthquake, *Bull. Seism. Soc. Amer.*, 1982, **72,** 1927–56.
41. Hartzell, S. & Helmberger, D. Strong-motion modeling of the Imperial Valley earthquake of 1979, *Bull. Seism. Soc. Amer.*, 1982, **72**(2), 571–96.
42. Hartzell, S. & Heaton, T. Inversion of strong ground motion and teleseismic wave form data for the fault rupture history of the 1979 Imperial Valley, California earthquake, *Bull. Seism. Soc. Amer.*, 1983, **73**(6), 1553–84.
43. Olson, A. & Aspel, R. Finite faults and inverse theory with applications to the 1979 Imperial Valley earthquake, *Bull. Seism. Soc. Amer.*, 1982, **72,** 1969–2002.
44. Trifunac, M.D. Stress estimates for San Fernando, California earthquake of February 9, 1971: main event and thirteen aftershocks, *Bull. Seism. Soc. Amer.*, 1972, **62,** 721–50.
45. Trifunac, M.D. Tectonic stress and source mechanism of the Imperial Valley, California earthquake of 1940, *Bull. Seism. Soc. Amer.*, 1972, **62,** 1283–302.
46. Trifunac, M.D. A three-dimensional dislocation model for the San Fernando, California, earthquake of February 9, 1971, *Bull. Seism. Soc. Amer.*, 1974, **64,** 149–72.
47. Wald, D., Helmberger, D.V. & Heaton, T.H. Rupture model of the 1989 Loma Prieta earthquake from the inversion of strong motion and broad band teleseismic data, *Bull. Seism. Soc. Amer.*, 1991, **81,** 1540–72.
48. Trifunac, M.D. & Udwadia, F.E. Parkfield, California, earthquake of June 27, 1966: a three-dimensional moving dislocation, *Bull. Seism. Soc. Amer.*, 1974, **64,** 511–33.
49. Scholz, C.H. Scaling laws for large earthquakes: consequences for physical models, *Bull. Seism. Soc. Amer.*, 1982, **72,** 1–14.
50. Trifunac, M.D. Broad band extension of Fourier amplitude spectra of strong motion acceleration, Department of Civil Engineering, Report No. CE 93-01, University of Southern California, Los Angeles, CA, 1993.
51. Trifunac, M.D. Fourier amplitude spectra of strong motion acceleration: extension to high and low frequencies, *Int. J. Earthqu. Engng Struct. Dynam.* (in press).
52. Savage, J.C. Relation of corner frequency to fault dimensions, *J. Geophys. Res.*, 1972, **77**(20), 3788–95.
53. Jovanovich, D., Husseini, M.I. & Chinnery, M.A. Elastic dislocations in a layered half space — I. Basic theory and numerical methods, *Geophys. J. R. Astr. Soc.*, 1974, **39,** 205–17.
54. Jovanovich, D., Husseini, M.I. & Chinnery, M.A. Elastic dislocation in a layered half space — II. Point source, *Geophys. J. R. Astr. Soc.*, 1974, **39,** 219–39.
55. Fletcher, J., Boatwright, J., Haar, L., Hanks, T. & McGarr, A. Source parameters for aftershocks of the Oroville, California, earthquake, *Bull. Seism. Soc. Amer.*, 1984, **74,** 1101–23.
56. Thatcher, W. & Hanks, T.C. Source parameters of Southern California earthquakes, *J. Geophys. Res.*, 1973, **78,** 8547–76.
57. Wyss, M. & Brune, J.N. Seismic moment, stress and source dimensions for earthquakes in California — Nevada region, *J. Geophys. Res.*, 1968, **73,** 4681–94.
58. Nuttli, O.W. Average seismic source parameter relation for mid-plate earthquakes, *Bull. Seism. Soc. Amer.*, 1983, **73**(2), 519–36.
59. Bakun, W.H. Seismic moments, local magnitudes, and coda-duration magnitudes for earthquakes in Central California, *Bull Seism. Soc. Amer.*, 1984, **74**(2), 439–58.
60. Bakun, W.H., Fuge, C.G. & Stewart, R.M. Body-wave spectra of Central California earthquakes, *Bull. Seism. Soc. Amer.*, 1976, **66,** 363–84.
61. Kanamori, H. & Anderson, D.L. Theoretical basis of some empirical relations in seismology, *Bull. Seism. Soc. Amer.*, 1975, **65,** 1073–95.

62. Vidal, A. & Munguia, L. Local magnitude and source parameters for earthquakes in the Peninsular Ranges of Baja California, *Bull. Seism. Soc. Amer.*, 1991, **81**(6), 2254–67.
63. Gutenberg, B. & Richter, C.F. Earthquake magnitude, intensity, energy and acceleration, *Bull. Seism. Soc. Amer.*, 1956, **46,** 105–45.
64. Chinnery, M.A. Earthquake magnitude and source parameters, *Bull. Seism. Soc. Amer.*, 1969, **59**(3), 1969–82.
65. Gibowicz, S.T. Stress drop and aftershocks, *Bull. Seism. Soc. Amer.*, 1973, **63,** 1433–46.
66. Hanks, T.C. & Wyss, M. The use of body wave spectra in the determination of seismic source parameters, *Bull. Seism. Soc. Amer.*, 1972, **62,** 561–89.
67. Wyss, M. & Molnar, P. Efficiency, stress drop, apparent stress, effective stress and frictional stress of Denver, Colorado earthquakes, *J. Geophys. Res.*, 1972, **77,** 1433–8.
68. Johnson, L.R. & McEvilly, T.V. Near field observations and source parameters of Central California earthquakes, *Bull. Seism. Soc. Amer.*, 1974, **64,** 1855–86.
69. O'Neill, M.E. & Healy, J.H. Determination of source parameters of small earthquakes from P wave rise time, *Bull. Seism. Soc. Amer.*, 1973, **63,** 101–4.
70. Chouet, B., Aki, K. & Tsujiura, M. Regional variation of the scaling law of earthquake source spectra, *Bull. Seism. Soc. Amer.*, 1978, **68,** 49–79.
71. Hanks, T.C. Observations and estimation of long-period strong ground motion in the Los Angeles Basin, preprint. 1975.
72. Hanks, T.C. & McGuire, R. K. The character of high frequency strong ground motion, *Bull. Seism. Soc. Amer.*, 1981, **71,** 2071–95.
73. Irikura, K. & Yokoi, T. Scaling law of seismic source spectra for the after shocks of 1983 Central-Japan-Sea earthquake, *Abstr. Seismol. Soc. Japan*, No. 1, 1984.
74. Somerville, P.G., McLaren, J.P., LeFerre, L.V., Burger, R.W. & Helmberger, D.V. Comparison of source scaling relations of eastern and western North American earthquakes, *Bull. Seism. Soc. Amer.*, 1987, **77,** 322–46.
75. Purcaru, G. & Berckhemer, H. Quantitative relations of seismic source parameters and a classification of earthquakes, *Tectonophysics*, 1982, **84,** 57–128.
76. Båth, M. & Duda, S.J. Earthquake volume, fault plane area seismic energy, strain, deformation and related quantities, *Ann. Geofis. (Rome)*, 1964, **17,** 353–68.